Tensor network influence functionals in the continuous-time limit: connections to quantum embedding, bath discretization, and higher-order time propagation

Gunhee Park,[1] Nathan Ng,[2] David R. Reichman,[2] and Garnet Kin-Lic Chan[3]

[1] *Division of Engineering and Applied Science, California Institute of Technology, Pasadena, CA 91125, USA*
[2] *Department of Chemistry, Columbia University, New York, New York 10027, United States*
[3] *Division of Chemistry and Chemical Engineering, California Institute of Technology, Pasadena, California 91125, USA*

We describe two developments of tensor network influence functionals (in particular, influence functional matrix product states (IF-MPS)) for quantum impurity dynamics within the fermionic setting of the Anderson impurity model. The first provides the correct extension of the IF-MPS to continuous time by introducing a related mathematical object, the boundary influence functional MPS. The second connects the dynamics described by a compressed IF-MPS to that of a quantum embedding method with a time-dependent effective bath undergoing non-unitary dynamics. Using these concepts, we implement higher-order time propagators for the quench dynamics of the Anderson impurity model within the boundary IF-MPS formalism. The calculations illustrate the ability of the current formulation to efficiently remove the time-step error in standard discrete-time IF-MPS implementations as well as to interface with state-vector propagation techniques. They also show the advantages of IF-MPS dynamics, with its associated highly compact effective bath dynamics, over state-vector propagation with a static bath discretization.

I. INTRODUCTION

Quantum impurity models, such as the Anderson impurity model (AIM), consist of an interacting impurity coupled to a (possibly non-interacting) bath. They provide simple settings in which to study quantum many-body physics, and the challenge of describing non-equilibrium dynamics in such models has spurred the development of many computational techniques [1–12].

One way to describe quantum impurity dynamics is to use the equation of motion of the impurity reduced density operator obtained by tracing out the bath. The influence of the bath is clearly expressed in a path integral language via the Feynman-Vernon influence functional (IF) [13], which reweights the paths in the path integral. Although the influence functional for a non-interacting bath with linear coupling can be expressed in a compact mathematical form, its effect on the impurity dynamics must still be numerically approximated in practice [14–25].

Recently, tensor network methods have been explored within the IF language to overcome some limitations of other numerical IF techniques, and in particular, to capture longer time memory effects [26–36]. By treating the IF as a temporal wavefunction expressed as a temporal matrix product state (MPS), one can exploit low entanglement in time, leading to a compact representation of certain temporal correlations. Such tensor network-based IF methods have been successfully demonstrated in several contexts, including the spin-boson model [28–32], hard-core bosons [31], one-dimensional spin chains [26, 27, 33], and more recently, in the context of the AIM [34–36].

The current work is concerned with two developments of the tensor network IF approach. Although the ideas generalize to IFs of any linearly-coupled non-interacting bath, for concreteness we work specifically with the AIM. The first development removes the time-step error in the standard IF treatment obtained from a Trotterized representation of the path integral. Formulating the problem in the continuous-time limit yields a continuous MPS version of the IF-MPS. We show that the standard IF-MPS in fact does not have a useful continuous-time limit, and instead one must consider a closely related object, the boundary IF-MPS, to define this limit. We provide an explicit construction of the continuous-time boundary IF-MPS for the AIM.

The second development is concerned with the relationship between the (boundary) IF-MPS and discrete bath dynamics. Standard state-vector methods for the dynamics of the AIM use a discrete bath with a fixed set of bath energies and couplings [1–5]. We show that impurity dynamics defined by an IF-MPS of fixed bond dimension is equivalent to propagating in a space of effective bath orbitals in Liouville space, where the bath energies and couplings dynamically vary with time. This naturally connects tensor network influence functionals to dynamical quantum embedding theories, such as real-time density matrix embedding, which also utilize a dynamical set of bath energies and couplings [37]. An important difference, however, is that the IF-MPS defines a non-unitary dynamics in the bath.

We implement the boundary IF-MPS propagation for the AIM in both the discrete-time and continuous-time formulations. Directly comparing to standard static bath discretizations, we show that the IF-MPS method converges extremely rapidly with respect to the effective bath size, and shows none of the discretization artifacts of standard bath discretizations. Further, the combination of the above two insights suggests that the boundary IF-MPS dynamics in the continuum limit can be efficiently implemented using standard state-vector time-propagation techniques. We use this to implement a

high-order Runge-Kutta time-propagator for boundary IF-MPS dynamics and demonstrate the high-order error with time-step. In contrast, we show that higher than first-order Trotter methods in the standard discrete-time IF-MPS still suffer from first-order time-step errors, due to the IF-MPS bond truncation. By Trotterizing the correct continuous-time dynamics, we derive a corrected version of the Trotterized error with the correct time-order scaling, significantly improving on the second-order Trotter formulation currently used in tensor network IF approaches.

The paper is organized as follows. In Sec. II, we first recapitulate the formulation of the IF-MPS for noninteracting fermionic baths, describing in detail the formalism we use here in terms of number-conserving Slater determinants. Through this picture, we establish the connection between the IF-MPS dynamics and Liouville state-vector propagation of an impurity coupled to a set of effective bath orbitals, that is, the dynamics of a quantum embedding of the impurity. In Sec. III, we analyze the continuous-time limit of the IF-MPS and show that the correct object to consider is the boundary IF-MPS and we provide its continuous-time limit. Using the state-vector formalism, we rewrite the continuous-time propagation in terms of a differential equation of motion for the Liouville state-vector in the quantum embedding space. In Sec. IV, we provide numerical results using the boundary IF-MPS for the single impurity Anderson model and compare the discretization errors associated with a static set of bath orbitals with the dynamic set of bath orbitals defined by the IF-MPS. We further analyze the time-step errors from both the discrete-time and continuous-time formulations. In Sec. V, we conclude with discussions of some implications of our results.

II. INFLUENCE FUNCTIONAL THEORY IN DISCRETE TIME

A. Influence Functional for Single Impurity Anderson Model

We consider a single impurity Anderson model,

$$\begin{aligned}\hat{H} &= \hat{H}_S + \hat{H}_{SB} + \hat{H}_B,\\ \hat{H}_S &= U\hat{n}_\uparrow\hat{n}_\downarrow + \sum_\sigma \varepsilon_\sigma \hat{n}_\sigma,\\ \hat{H}_{SB} &= \sum_{i,\sigma}\left(t_i\hat{c}^\dagger_{i,\sigma}\hat{d}_\sigma + \text{h.c.}\right),\\ \hat{H}_B &= \sum_{i,\sigma} E_i \hat{c}^\dagger_{i,\sigma}\hat{c}_{i,\sigma},\end{aligned} \tag{1}$$

where $\hat{d}^\dagger_\sigma$ ($\hat{c}^\dagger_{i,\sigma}$) creates a fermion of spin $\sigma \in \{\uparrow,\downarrow\}$ in the impurity (bath) orbitals and $\hat{n}_\sigma = \hat{d}^\dagger_\sigma\hat{d}_\sigma$ is the number density operator of the impurity orbital of spin σ. Note that $\hat{H}_{SB}$ and $\hat{H}_B$ are of noninteracting (quadratic) form. Hereafter, we assume a discrete and finite set of bath orbitals and also assume that the impurity is initially decoupled from the bath, $\hat{\rho}(0) = \hat{\rho}_S(0)\otimes\hat{\rho}_B$. We further assume a Gaussian initial bath, in particular, the thermal state $\hat{\rho}_B \propto e^{-\beta\hat{H}_B}$ with inverse temperature β. For quadratic operators, we omit the hats when expressing their matrix elements in a single-particle basis.

While the time evolution of the density operator can be described by the von Neumann equation,

$$i\frac{d}{dt}\hat{\rho} = [\hat{H},\hat{\rho}], \tag{2}$$

we instead will adopt the super-fermion representation of Liouville space [17, 38–41]. This uses a super-Fock space with twice the number of orbitals as the original Hilbert space, obtained by applying a particle-hole transformation to the bra of the density operator, and assuming the resulting operator acts on a vacuum to produce a state. We denote states in the super-Fock space using a double bra/ket notation. For example, the initial density operator is written as $|\rho(0)\rangle\!\rangle = |\rho_S(0)\rangle\!\rangle\otimes|\rho_B\rangle\!\rangle$. The von Neumann equation now becomes a Hamiltonian time evolution with the Liouville operator, $\hat{L}$,

$$i\frac{d}{dt}|\rho\rangle\!\rangle = \hat{L}\,|\rho\rangle\!\rangle\,. \tag{3}$$

The Liouville operator for the Anderson impurity model takes the form (using tildes on the operators from the particle-hole transformed Fock space),

$$\begin{aligned}\hat{L} &= \hat{L}_S + \hat{L}_{SB} + \hat{L}_B,\\ \hat{L}_S &= U\hat{n}_\uparrow\hat{n}_\downarrow - U(1-\hat{\tilde{n}}_\uparrow)(1-\hat{\tilde{n}}_\downarrow)\\ &\quad + \sum_\sigma \varepsilon_\sigma(\hat{n}_\sigma + \hat{\tilde{n}}_\sigma),\\ \hat{L}_{SB} &= \sum_{i,\sigma}\left(t_i\hat{c}^\dagger_{i,\sigma}\hat{d}_\sigma + t_i\hat{\tilde{c}}^\dagger_{i,\sigma}\hat{\tilde{d}}_\sigma + \text{h.c.}\right),\\ \hat{L}_B &= \sum_{i,\sigma} E_i(\hat{c}^\dagger_{i,\sigma}\hat{c}_{i,\sigma} + \hat{\tilde{c}}^\dagger_{i,\sigma}\hat{\tilde{c}}_{i,\sigma}),\end{aligned} \tag{4}$$

where we have omitted all constant terms. We will collectively refer to the tilde and non-tilde creation operators as $\hat{a}^\dagger_{i,\sigma}$,

$$\hat{a}^\dagger_{i,\sigma} = \begin{cases}\hat{c}^\dagger_{i,\sigma} & 1\le i\le N_b\\ \hat{\tilde{c}}^\dagger_{i-N_b,\sigma} & N_b+1\le i\le 2N_b\end{cases}, \tag{5}$$

for N_b bath orbitals.

The initial bath state in the super-Fock space, $|\rho_B\rangle\!\rangle$, is given by a Slater determinant

$$|\rho_B\rangle\!\rangle = \prod_{i,\sigma}\left(f_+(E_{i,\sigma},\beta)\hat{c}^\dagger_{i,\sigma} + f_-(E_{i,\sigma},\beta)\hat{\tilde{c}}^\dagger_{i,\sigma}\right)|0\rangle\!\rangle \tag{6}$$

where $|0\rangle\!\rangle$ is a vacuum state in the super-Fock space, $f_+(E,\beta) = (1+e^{\beta E})^{-1}$, and $f_-(E,\beta) = 1 - f_+(E,\beta)$.

We are often interested in the reduced density operator of the impurity, $\hat{\rho}_S = \mathrm{Tr}_B(\hat{\rho})$. In the super-Fock space, the trace over the bath is equivalent to taking the overlap with a trace vector that can be expressed as a Slater determinant,

$$|\mathrm{Tr}_B\rangle\!\rangle = \prod_{i,\sigma} \left(\hat{c}^\dagger_{i,\sigma} + \hat{\tilde{c}}^\dagger_{i,\sigma}\right)|0\rangle\!\rangle\,, \tag{7}$$

and the amplitude of a configuration s in ρ_S can be expressed as,

$$\langle\!\langle s|\rho_S\rangle\!\rangle = \left(\langle\!\langle s| \otimes \langle\!\langle \mathrm{Tr}_B|\right)|\rho\rangle\!\rangle\,. \tag{8}$$

The discretized time evolution of the density operator with timestep Δt can be expressed via a second-order Trotter decomposition

$$\begin{aligned}|\rho_S(t_N)\rangle\!\rangle &= \mathrm{Tr}_B\left[\left(e^{-\frac{i}{2}\hat{L}_S\Delta t}e^{-i\hat{L}_{SB}\Delta t}e^{-\frac{i}{2}\hat{L}_S\Delta t}\right)^{N_t}|\rho(0)\rangle\!\rangle\right] \\ &= \mathrm{Tr}_B\left[\hat{U}^S\hat{U}^{SB}\hat{U}^S\cdots\hat{U}^{SB}\hat{U}^S\,|\rho(0)\rangle\!\rangle\right]\end{aligned} \tag{9}$$

where $t_{N_t} = N_t\Delta t$ and $\hat{U}^S$ ($\hat{U}^{SB}$) is the time evolution operator for $\hat{L}_S$ ($\hat{L}_{SB}$ and $\hat{L}_B$). The tensor network diagram for this time evolution is shown in Fig. 1, where we see that the $\hat{U}^S$ tensor is applied only within the impurity S, whereas the tensor for $\hat{U}^{SB}$ is applied to both S and B.

The influence functional (IF) tensor is defined as the tensor arising from the contraction of all the bath degrees of freedom in $\hat{U}_{SB}$, the initial bath density operator, and the trace vector (Fig. 1). This IF tensor is indexed by the state of the impurity orbitals before and after each $\hat{U}_{SB}$, for N_t time-steps (denoted s^i_m and s^f_m, respectively, for the m-th time-step) and so is indexed by the configuration of $2N_t$ impurity orbitals. In addition, we mention that the IF tensors for different spins are constructed separately thanks to the absence of spin-mixing terms in $\hat{L}_{SB}$, and hence, the spin indices are omitted for brevity.

Due to the one-dimensional structure of the temporal axis, the IF can be rewritten in terms of N_t tensors that are directly obtained from $\hat{U}^{SB}$ by inserting the bath configurations between each time-step. Denoting the impurity configurations, $\boldsymbol{s} = (s^i_1, s^f_1, \cdots, s^i_{N_t}, s^f_{N_t})$, and the corresponding IF tensor element as $I(\boldsymbol{s})$, the matrix product state (MPS) representation of the IF can be written as,

$$I(\boldsymbol{s}) = l^T \cdot A^{s^i_{N_t},s^f_{N_t}}_{N_t}\cdots A^{s^i_1,s^f_1}_1 \cdot r, \tag{10}$$

where the matrix elements for A_m are given by

$$\left(A^{s^i_m,s^f_m}_m\right)_{b_m,b_{m-1}} = \langle\!\langle s^f_m, b_m|\,\hat{U}^{SB}\,|s^i_m, b_{m-1}\rangle\!\rangle\,, \tag{11}$$

and b_m is the bath configuration after m applications of $\hat{U}^{SB}$, $r_{b_0} = \langle\!\langle b_0|\rho_B(0)\rangle\!\rangle$, and $l_{b_{N_t}} = \langle\!\langle \mathrm{Tr}_B\,|b_{N_t}\rangle\!\rangle$.

In the above MPS representation, the bond dimension is given by the dimension of the super-Fock bath space, which, in many cases, is too large to deal with directly. Previous studies [35, 36] have made use of the fermionic Gaussian properties of the IF (arising from the linear coupling and quadratic bath) to find a compressed form of the MPS representation [42, 43]. In this work, we will use a slightly different language to formulate the MPS compression in terms of finding Schmidt vectors in the bath. This algorithm (described in Sec. II E) is closely related to that in Ref. [42] and improves on the computational scaling in Ref. [43].

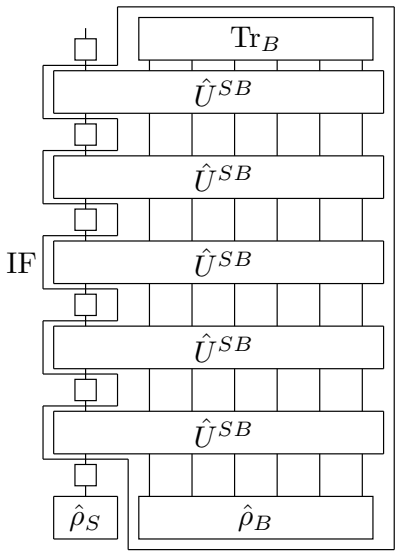

FIG. 1. A schematic diagram for the real-time evolution of the Anderson Impurity model in Liouville space after $N_t = 5$ time-steps. The initial density operator is given by $\hat{\rho}(0) = \hat{\rho}_S \otimes \hat{\rho}_B$, described by a vectorized state in a Liouville space. The time evolution of the density operator is described by time evolution operators following a second-order Trotter decomposition, alternating between $\hat{U}^S$ (squares) and $\hat{U}^{SB}$ (rectangles). After the time evolution, the bath degrees of freedom are traced out, which is equivalent to applying the trace tensor, Tr_B, to the bath. The influence functional (IF) tensor corresponds to the tensor after the contraction of the bath modes in all $\hat{U}^{SB}$, $\hat{\rho}_B$, and Tr_B tensors.

B. From Influence Functionals to State-Vector Propagation

In this work, we will often switch between two equivalent pictures: dynamics encoded by a compressed IF-MPS, and a state-vector propagation corresponding to a quantum embedding. To understand this mapping, we first describe the conventional MPS compression scheme (i.e. without using any Gaussian properties of the bath) and explain how it can be interpreted as a type of projected bath dynamics. (We recall that the IF-MPS can, in general, be expressed through Eq. 10 and 11, for arbitrary system-bath quantum dynamics, i.e. even for an interacting bath).

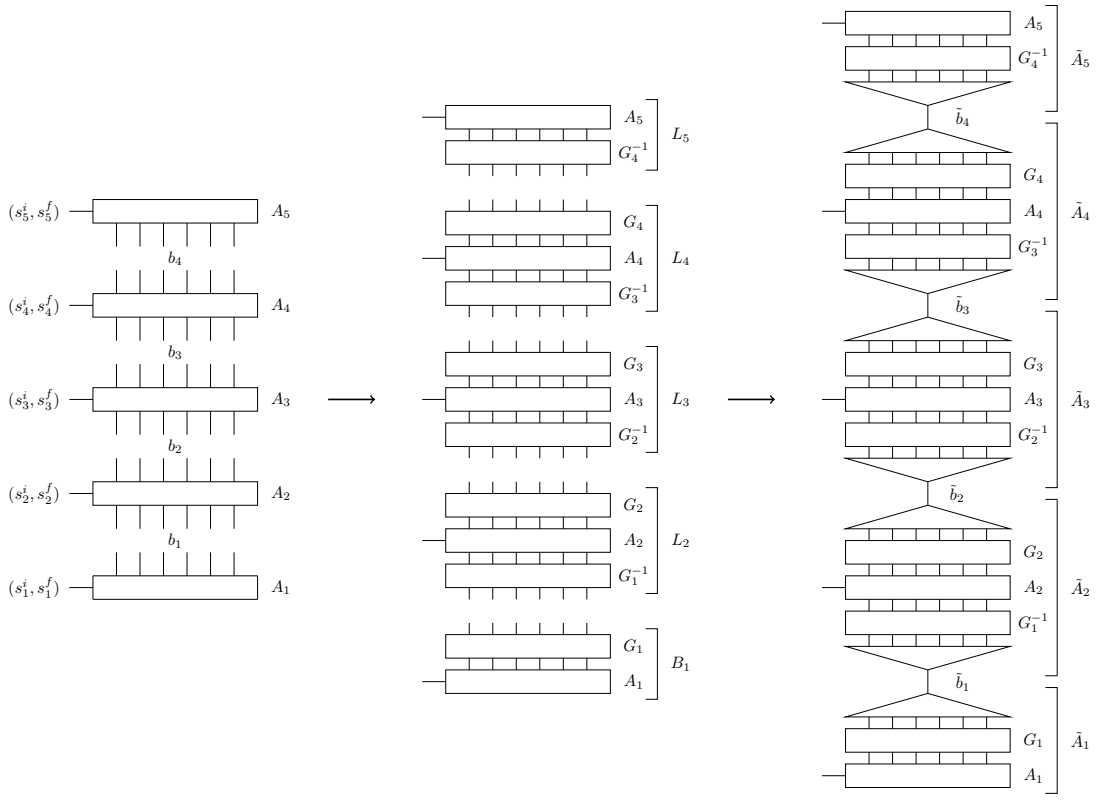

FIG. 2. General matrix product state (MPS) compression scheme for an influence functional MPS (IF-MPS). The bond dimension of the initial uncompressed MPS is given by the dimension of the bath Liouville space, indexed by bath configurations, b_m (left). The MPS needs to be converted into canonical form for an optimal truncation. The gauge matrices, G_m, are inserted in the bath Liouville space to convert the MPS into the canonical form (middle). Gauge matrices transform the original matrix elements of the MPS into left-normalized matrices, denoted as $L_m = G_m A_m G_{m-1}^{-1}$. Afterward, projectors are inserted into the bath subspace that contains the bath states with the largest singular values (right). The projected bath configurations are denoted as $\tilde{b}_m$.

In conventional MPS compression, the MPS is first transformed to a canonical form to enable an optimal truncation of the bond dimension. The canonical form is defined using the gauge degrees of freedom in the MPS [44],

$$A_m^{s_m^i, s_m^f} \to L_m^{s_m^i, s_m^f} = G_m A_m^{s_m^i, s_m^f} G_{m-1}^{-1}, \tag{12}$$

$$\sum_{s_m^i, s_m^f} L_m^{s_m^i, s_m^f \dagger} L_m^{s_m^i, s_m^f} = I, \tag{13}$$

where the matrices, $L_m^{s_m^i, s_m^f}$, satisfying Eq. 13, are called left-normalized matrices. The gauge matrices, G_m, are inserted in the bond space, or the Liouville bath space of the IF-MPS (Fig. 2). The MPS that is composed of the left-normalized matrices is called left-canonical. The left-canonical MPS is then

$$I(\boldsymbol{s}) = L_{N_t}^{s_{N_t}^i, s_{N_t}^f} \cdots L_2^{s_2^i, s_2^f} B_1^{s_1^i, s_1^f}, \tag{14}$$

where $B_1^{s_1^i, s_1^f} = G_1 A_1^{s_1^i, s_1^f}$. After choosing this gauge, the MPS is compressed by iteratively applying truncated singular value decompositions (SVD) from right to left.

We can group together the effect of the gauging and compression together with the system-bath evolution to define new matrices of the IF-MPS, $\tilde{A}_m$,

$$\left(\tilde{A}_m^{s_m^i, s_m^f}\right)_{\tilde{b}_m, \tilde{b}_{m-1}} = \left\langle\!\left\langle s_m^f, \tilde{b}_m \right| \mathcal{P}_m \hat{G}_m \hat{U}^{SB} \hat{G}_{m-1}^{-1} \mathcal{P}_{m-1} \left| s_m^i, \tilde{b}_{m-1} \right\rangle\!\right\rangle, \tag{15}$$

where $\mathcal{P}_m$ denotes the projectors onto the bath states associated with the largest singular values (or equivalently, the largest eigenvalues of the bath density matrix) after the gauge transformation (Fig. 2), and $\tilde{b}_m$ denotes the projected bath configurations.

$\tilde{A}_m$ can be viewed as defining a (non-unitary) evolution in the Liouville space of the system and the bath. Alternatively, the MPS gauging and compression procedure can be seen as a pure projected bath dynamics in the Liouville space, $\hat{G}_m^{-1} \mathcal{P}_m \hat{G}_m$, inserted between the system-bath evolution $\hat{U}^{SB}$. The coarse-graining (i.e. projection) of the bath degrees of freedom is referred to as a quantum embedding, and consequently, the truncated IF-MPS dynamics is a quantum embedding scheme with a dynamically evolved bath, similar to (real-time) den-

sity matrix embedding theory (DMET) [37, 45–47], but with the important difference that the dynamics of the projected bath is non-unitary, as $\hat{G}_m$ is non-unitary.

As the time-step $\Delta t \to 0$, we are led to the continuous-time limit of the IF-MPS. We consider the subtleties of continuous-time construction in Sec. III A. However, the above shows that we can also view time evolution as being performed on an embedded state-vector ("wavefunction") in the projected Liouville space (embedding space) $\{|s_m^i \tilde{b}_m\rangle\rangle\}$. We can then formulate the continuous-time dynamics in terms of the equations of motion for the embedded wavefunction and the bath projectors (or equivalently, the bath density matrix). The dynamics of such a bath density matrix has previously been considered in the MPS language in Ref. [27] for a 1D spin chain, which derived the dissipative contribution of the system-bath coupling to the density matrix dynamics.

We will be interested in the above constructions for the case of a fermionic Gaussian bath where we can replace the discussion of many-body states and density matrices with orbitals and 1-particle reduced density matrices (1-RDM). We now turn to the formulation of the IF-MPS operations in terms of these quantities.

C. Schmidt Decomposition of Slater determinants

In this section, we review the Schmidt decomposition of Slater determinants [46, 48]. A Slater determinant is given by

$$|\psi\rangle = \prod_{p=1}^{N_{\text{occ}}} \hat{c}_p^\dagger |0\rangle, \quad \hat{c}_p^\dagger = \sum_i C_{ip} \hat{a}_i^\dagger \tag{16}$$

where $\hat{c}_p^\dagger$ is a creation operator of the N_{occ} occupied orbitals, $\hat{a}_i^\dagger$ is a creation operator of orthonormal orbitals in the basis of n sites, and C_{ip} is the orbital coefficient matrix. Given a bipartite Hilbert space, $\mathcal{H} = \mathcal{H}_A \otimes \mathcal{H}_B$, where the first n_A orbitals belong to subsystem A and the other $n_B = n - n_A$ orbitals belong to subsystem B, the Schmidt decomposition of the Slater determinant can be obtained by diagonalizing the one-particle reduced density matrices (1-RDM), $\Gamma_{ij} = \langle\psi| \hat{a}_j^\dagger \hat{a}_i |\psi\rangle$, of the subsystems. Assuming $n_A < n_B$ and $N_{\text{occ}} > n_A$, the Schmidt decomposition can be written as,

$$|\psi\rangle = \prod_{k=1}^{n_A} \left(\sqrt{\nu_k}\hat{c}_{A,k}^\dagger + \sqrt{1-\nu_k}\hat{c}_{B,k}^\dagger\right) \prod_{l=n_A+1}^{N_{\text{occ}}} \hat{c}_{B,l}^\dagger |0\rangle \tag{17}$$

where ν_k $(1-\nu_k)$ denote the eigenvalues of the 1-RDM of A (B) with values between 0 and 1, $\hat{c}_{A,k}^\dagger$ $(\hat{c}_{B,k}^\dagger)$ create the corresponding eigenmodes, and $\hat{c}_{B,l}^\dagger$ create eigenmodes with eigenvalue 1 of the 1-RDM of B.

Based on the above, the orbitals in B can be classified into three different categories: (1) *entangled* orbitals, $\hat{c}_{B,k}^\dagger$, $1 \le k \le n_A$, which are entangled with A, (2) *core* orbitals, $\hat{c}_{B,l}^\dagger$, $n_A + 1 \le l \le N_{\text{occ}}$, which are fully occupied in B and not entangled with A, (3) *virtual* orbitals, which are unoccupied and so do not appear in Eq. 17 and also are not entangled with A.

Note that the Slater determinant with all $\nu_k = \frac{1}{2}$ corresponds to a maximally entangled fermionic state, $|\phi\rangle$, where the reduced density operator of subsystem A is proportional to the identity. It is possible to write the 1-RDM of A from $|\psi\rangle$ as that of a maximally entangled fermionic state $|\phi\rangle$ after a gauge transformation within the subsystem A, i.e. $\hat{G}_A |\phi\rangle$, where

$$\hat{G}_A = \exp\left(\sum_k \log g_k \hat{c}_{A,k}^\dagger \hat{c}_{A,k}\right), \quad g_k = \sqrt{\frac{\nu_k}{1-\nu_k}}, \tag{18}$$

up to a normalization constant factor, assuming $0 < \nu_k < 1$ for all k. $\hat{G}_A$ satisfies the following

$$\hat{G}_A \hat{c}_{A,k}^\dagger \hat{G}_A^{-1} = g_k \hat{c}_{A,k}^\dagger, \; \hat{G}_A \hat{c}_{A,k} \hat{G}_A^{-1} = g_k^{-1} \hat{c}_{A,k} \tag{19}$$

This gauge transformation is related to the gauge transformation introduced in Sec. II B because the state $|\phi\rangle$ is 'left-normalized' with respect to the subsystem A. We will use this gauge transformation to convert Slater determinants into left-normalized forms in the next section.

The Schmidt decomposition can be truncated by treating the entangled orbitals with $\nu_k \approx 1$ $(\nu_k \approx 0)$ as core (virtual) orbitals, retaining the orbitals with larger $\sqrt{\nu_k(1-\nu_k)}$. In other words, a projection operator on the entangled orbital space that keeps only ν_k close to $\frac{1}{2}$ can be applied to truncate the Schmidt decomposition. This truncation scheme is sometimes called a "mode" truncation [42, 49, 50] and has been utilized in the context of tensor network truncations of fermionic Gaussian states.

After a truncation to n_{ent} entangled orbitals, the Slater determinant can be written as,

$$|\psi\rangle = \prod_{k=1}^{n_{\text{ent}}} \left(\sqrt{\nu_k}\hat{c}_{A,k}^\dagger + \sqrt{1-\nu_k}\hat{c}_{B,k}^\dagger\right) \times \prod_{l=n_{\text{ent}}+1}^{n_{\text{ent}}+n_{A,c}} \hat{c}_{A,l}^\dagger \prod_{l=n_{\text{ent}}+1}^{n_{\text{ent}}+n_{B,c}} \hat{c}_{B,l}^\dagger |0\rangle, \tag{20}$$

where $n_{A,c}$ $(n_{B,c})$ is the number of core orbitals in A (B).

D. Influence Functional tensors as Slater determinants

We now describe how the bipartitions of the exact influence functional tensor can be expressed as Slater determinants, which are obtained by propagating a finite number of steps forward in time from $|\rho_B(0)\rangle\rangle$ or backward in time from $\langle\langle \text{Tr}_B|$. Thanks to the noninteracting nature of the bath, both the IF and its partitions correspond to fermionic Gaussian states, specifically, Bardeen-Cooper-Schrieffer (BCS) states [34–36]. Despite this fact, we will

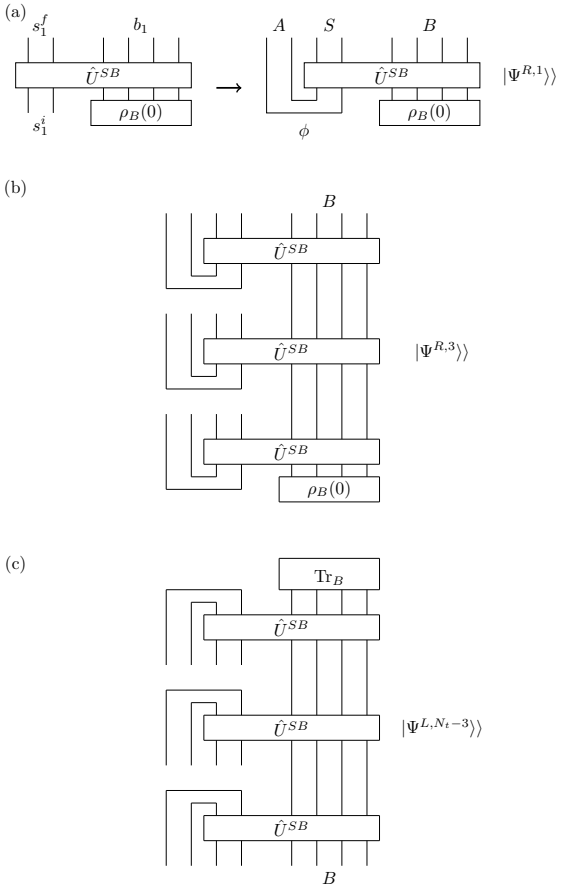

FIG. 3. (a) A right IF state after one time-step, $|\Psi^{R,1}\rangle\rangle$. It represents a partial contraction of the bath degrees of freedom between the time evolution operator, $\hat{U}^{SB}$, and the initial bath density operator, $\rho_B(0)$. It can be expressed as a Slater determinant by introducing a maximally entangled fermionic state, ϕ, which has impurity and auxiliary fermionic orbitals denoted by S and A, respectively. Coupling the maximally entangled state to the time evolution operator on the input impurity orbitals yields the Slater determinant state. (b) A right IF state after the m-th time-step, $|\Psi^{R,m}\rangle\rangle$, ($m = 3$ in the figure) can also be represented as a Slater determinant by introducing maximally entangled fermionic states at each time-step. (c) A left IF state, $|\Psi^{L,m}\rangle\rangle$, ($m = N_t - 3$ in the figure) can be constructed by contracting the time evolution operator from the top downwards, and can also be represented as a Slater determinant by inserting maximally entangled fermionic states starting from the top.

prefer to work with Slater determinants and convert the BCS states to Slater determinants through a particle-hole transformation. This is because when building the matrix elements of the IF-MPS in Eq. 15, the basis of Slater determinants will allow us to use number symmetry, which significantly reduces the prefactors in the numerical computations.

We define the right and left bipartitions of IF (right and left IF for short) $\prod_m \hat{U}_m^{SB} \cdot |\rho_B(0)\rangle\rangle$ and $\langle\langle \mathrm{Tr}_B| \cdot \prod_m \hat{U}_m^{SB}$, respectively, where the products follow the order in the MPS representation and here, $\cdot$ indicates the partial contraction of the intermediate bath configurations. We start with the first right IF, $\hat{U}^{SB} \cdot |\rho_B(0)\rangle\rangle$ for simplicity. Its tensor elements are determined from $\langle\langle s_1^f, b_1| \hat{U}^{SB}(|s_1^i\rangle\rangle \otimes |\rho_B(0)\rangle\rangle)$, and its external degrees of freedom are s_1^i, s_1^f, and b_1 (see Fig. 3(a)). Its occupation numbers satisfy the relationship,

$$n(s_1^f) + n(b_1) - n(s_1^i) = n(\rho_B(0)), \tag{21}$$

which is not consistent with a number-conserving state.

After applying the particle-hole transformation to the input configuration, $s_1^i \to \bar{s}_1^i$, (for example, $00 \to 11$, $01 \to 10$, $10 \to 01$, and $11 \to 00$), we obtain,

$$n(s_1^f) + n(b_1) + n(\bar{s}_1^i) = n(\rho_B(0)) + 2, \tag{22}$$

where $n(\bar{s}_1^i) = 2 - n(s_1^i)$. Therefore, after the transformation, the right partition IF is a Slater determinant with $n(\rho_B(0)) + 2$ occupied orbitals.

Formally, the particle-hole transformations can be expressed in terms of fermionic tensor network contractions by inserting maximally entangled fermionic states,

$$|\phi\rangle\rangle = \prod_s \frac{1}{\sqrt{2}}(\hat{\alpha}_s^\dagger + \hat{d}_s^\dagger)\,|0\rangle\rangle\,, \tag{23}$$

where the index s denotes the input impurity orbitals from the super-Fock Liouville space and $\hat{\alpha}_s^\dagger$ indicates a creation operator of auxiliary fermionic orbitals. Note that the occupation numbers of the auxiliary fermionic orbitals have particle-hole transformed occupation numbers compared to the original input impurity orbitals. The right IF state representation of $\hat{U}^{SB} \cdot |\rho_B(0)\rangle\rangle$, which we will denote $|\Psi^R\rangle\rangle \equiv |\Psi^{R,1}\rangle\rangle$, is then written as follows (Fig. 3a),

$$|\Psi^{R,1}\rangle\rangle = \left(\hat{I}^A \otimes \hat{U}^{SB}\right)|\phi\rangle\rangle \otimes |\rho_B(0)\rangle\rangle\,, \tag{24}$$

where $\hat{I}^A$ is the identity operator on the auxiliary fermionic orbitals. Because the initial state, $|\phi\rangle\rangle \otimes |\rho_B(0)\rangle\rangle$ is given by a Slater determinant and $\hat{I}^A \otimes \hat{U}^{SB}$ is number-conserving, we see again that the right IF state is also a Slater determinant. The right IF state for $\prod_m \hat{U}_m^{SB} \cdot |\rho_B(0)\rangle\rangle$ can be similarly expressed by inserting maximally entangled fermionic states at each time-step and coupling one of the modes to $\hat{U}^{SB}$, as shown schematically in Fig. 3b.

To construct the compression of the IF-MPS later, we require the bath 1-RDMs. Given the right IF state at the m-th time-step, $|\Psi^{R,m}\rangle\rangle$, we define the bath 1-RDM of the right IF state (Fig. 4a) as,

$$\Gamma_{ij}^{R,m} = \frac{\langle\langle \Psi^{R,m}|\, \hat{a}_j^\dagger \hat{a}_i\, |\Psi^{R,m}\rangle\rangle}{\langle\langle \Psi^{R,m}|\Psi^{R,m}\rangle\rangle}, \tag{25}$$

where the indices i and j refer to the super-Fock bath orbitals. The 1-RDM at the next time-step can be computed from the evolution of $|\phi\rangle\rangle \otimes |\Psi^{R,m}\rangle\rangle$ under $\hat{I}^A \otimes \hat{U}^{SB}$.

The bath 1-RDM after the evolution can be written as,

$$\Gamma^{R,m+1}_{ij} = \left[U^{SB}\Gamma^{R,m}U^{SB\dagger}\right]_{ij} + \left[U^{ASB}\Gamma^{\phi}U^{ASB\dagger}\right]_{ij}, \tag{26}$$

where Γ^{ϕ} denotes the 1-RDM of $|\phi\rangle\rangle$ and U^{ASB} denotes a single particle-basis representation of $\hat{I}^A \otimes \hat{U}^{SB}$. The diagrammatic representation of the evolution of the bath 1-RDM is drawn in Fig. 4b.

We can construct the left IF state in an analogous way, but where the state propagates in the inverse (negative) time direction using $\hat{U}^{SB\dagger}$ (Fig. 4c). Denoting the left IF state and its bath 1-RDM, $|\Psi^L\rangle\rangle$ and Γ^L, respectively, the bath 1-RDMs at successive time-steps (from top downwards) are related by

$$\Gamma^{L,m-1}_{ij} = \left[U^{SB\dagger}\Gamma^{L,m}U^{SB}\right]_{ij} + \left[U^{ASB\dagger}\Gamma^{\phi}U^{ASB}\right]_{ij}, \tag{27}$$

Note that the initial state is given by the trace vector, $|\Psi^{L,N_t}\rangle\rangle = |\mathrm{Tr}_B\rangle\rangle$, which is also given by a Slater determinant as in Eq. 7. With both the left and right IF state, the IF-MPS can be written as $\langle\langle\Psi^{L,m}| \cdot |\Psi^{R,m}\rangle\rangle$ for any m.

E. Influence Functional Matrix Product State Compression

We now revisit the MPS compression of the IF-MPS, described in Sec. II B, but now utilizing the non-interacting nature of the bath, which allows all the steps to be expressed at the level of orbitals and single-particle quantities.

In Sec II B, the optimal compression of the MPS required the IF-MPS to be in a canonical form. This was achieved by transforming matrices into left-normalized matrices by inserting gauge matrices into the MPS. As discussed in Sec. II D the partitions of the IF-MPS for a non-interacting bath are Slater determinants, and the gauge transformation (Eq. 18) to convert Slater determinants to maximally entangled fermionic pairs, which are left-normalized, was introduced in Sec. II C.

We therefore have all the ingredients to convert the IF-MPS to canonical form. We start with the left IF state, $|\Psi^L\rangle\rangle$, and determine the gauge transformation, $\hat{G}$, from the eigenvalues and eigenvectors of the bath 1-RDM, Γ^L_{ij}. We denote the eigenvalues of Γ^L_{ij} as ν_k, where k indexes the eigenvalues, and the rotation matrix as R^L_{ik}, whose columns are the eigenvectors of Γ^L in a single-particle basis. With this gauge transformation, we can represent the IF-MPS as, $\langle\langle\Psi^L| \cdot |\Psi^R\rangle\rangle = \langle\langle\phi| \cdot \hat{G} \cdot |\Psi^R\rangle\rangle$. The gauge matrix in the single-particle basis, G, can be written as,

$$G_{ki} = g_k R^{L*}_{ik}, \tag{28}$$

where $g_k = \sqrt{\nu_k/(1-\nu_k)}$ (Eq. 18). Note that g_k diverges when $\nu_k \to 1$, so in practice, we regularize ν_k with a small threshold ε so that $\nu_k = \varepsilon$ when $\nu_k < \varepsilon$ and $\nu_k = 1-\varepsilon$ when $1-\nu_k < \varepsilon$. A similar regularization scheme for the 1-RDM has been used in multiconfiguration time-dependent Hartree theory [51, 52] and real-time density matrix embedding theory [37, 47].

The gauge matrices need to be absorbed into the right IF state to further canonicalize the IF-MPS. We call the state, $|\Psi^G\rangle\rangle = \hat{G} \cdot |\Psi^R\rangle\rangle$, a gauge-transformed right IF state and its bath 1-RDM, Γ^G. The gauge transformation is a non-unitary transformation, so we always normalize the state when computing Γ^G.

$$\begin{aligned}\Gamma^G_{ij} &= \frac{\langle\langle\Psi^G|\, \hat{a}^\dagger_j \hat{a}_i \,|\Psi^G\rangle\rangle}{\langle\langle\Psi^G|\Psi^G\rangle\rangle} \\ &= \left[G\sqrt{\Gamma^R}(\sqrt{\Gamma^R}G^\dagger G\sqrt{\Gamma^R} + I - \Gamma^R)^{-1}\sqrt{\Gamma^R}G^\dagger\right]_{ij}\end{aligned} \tag{29}$$

where Γ^R is the bath 1-RDM of the $|\Psi^R\rangle\rangle$. A detailed derivation of this expression is included in the Supplemental Material.

Subsequently, we decompose the gauge-transformed right IF state into a right-normalized maximally entangled fermionic state and another gauge transformation, and this gauge transformation contains the singular values of the IF-MPS at this bipartition. Taking the largest singular values in the truncated SVD in the conventional MPS compression is equivalent to taking the eigenvectors of Γ^G with eigenvalues closest to $\frac{1}{2}$ (or large $\nu^G_k(1-\nu^G_k)$) as done in the mode truncation approach introduced in Sec. II C. We will call the bath orbitals from the selected eigenvectors of Γ^G the effective bath orbitals.

Hence, the procedure for IF-MPS compression at the orbital level is as follows: (1) Diagonalize the bath 1-RDM of the gauge-transformed right IF state, Γ^G, and obtain its eigenvalues, ν^G_k, and rotation matrix, R^G. (2) Take the eigenvectors with the N_{eff} largest $\nu^G_k(1-\nu^G_k)$, where N_{eff} is a number of the effective bath orbitals we select, defining the truncated rotation matrix R^{eff}. (3) Construct the projection operator, $\mathcal{P}$, from R^{eff}, i.e. the eigenvectors corresponding to the effective bath orbitals. The configurations from the other bath orbitals in the projected subspace are fixed to be either fully occupied (core orbitals, $\nu^G_k \approx 1$) or unoccupied (virtual orbitals, $\nu^G_k \approx 0$).

For the Liouville time evolution of the Anderson impurity model with the initial Gaussian thermal bath, it is possible to prove that if ν^G_k is an eigenvalue of Γ^G, so is $1-\nu^G_k$ (Supplemental Material). In this case, we obtain the same number of core and virtual orbitals and choose the effective bath orbitals symmetrically by occupancy.

The tensor elements of the IF-MPS can then be computed from Eq. 15, after applying the gauge transformation and the projectors, $\mathcal{P}_m$, for each m-th time-step,

$$\langle\langle s^f_m, \tilde{b}_m|\, \mathcal{P}_m \hat{G}_m \hat{U}^{SB} \hat{G}^{-1}_{m-1} \mathcal{P}_{m-1} \,|s^i_m, \tilde{b}_{m-1}\rangle\rangle, \tag{30}$$

with the configurations of the effective bath orbitals, $\tilde{b}_m$. This tensor element defines an effective time evolution operator for the embedded wavefunction defined on the impurity and effective bath orbitals. The diagrammatic

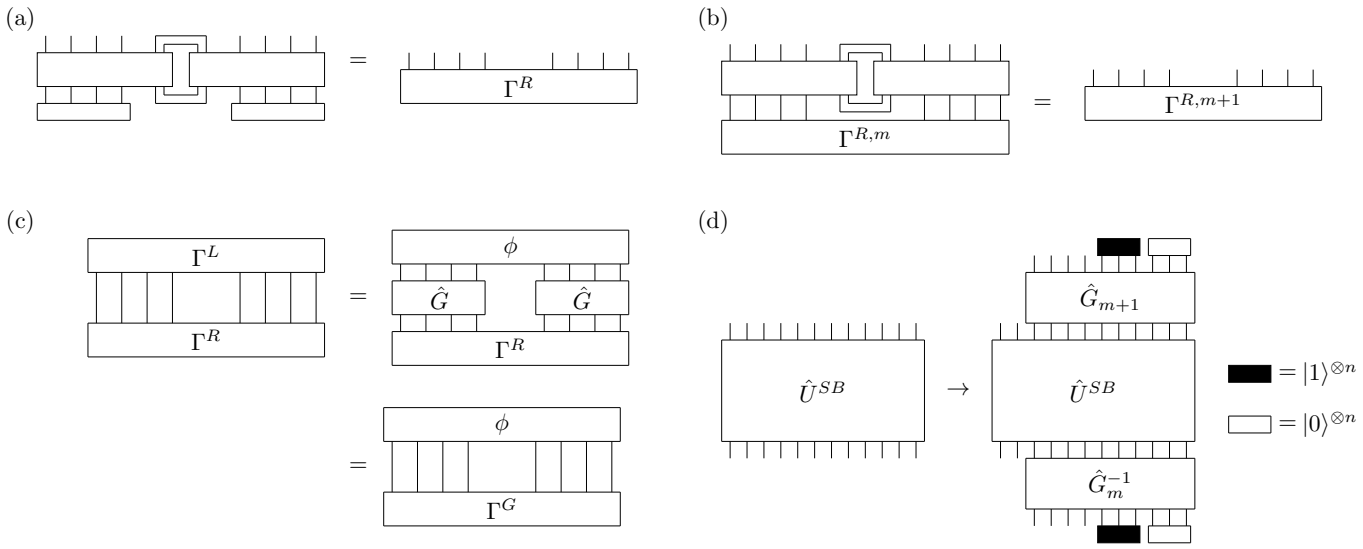

FIG. 4. **(a)** The bath 1-RDM of the right IF state, Γ^R, is obtained by tracing out the impurity orbitals, i.e. by contracting the state with its complex conjugate, within the impurity space. **(b)** The bath 1-RDM of the right IF state after the m-th time-step, $\Gamma^{R,m}$ can be updated to $\Gamma^{B,m+1}$ by applying the time evolution operator and tracing out the impurity orbitals. **(c)** A gauge transformation, $\hat{G}$, is extracted from the bath 1-RDM of the left IF state, Γ^L, by converting it to a maximally entangled fermionic state, ϕ. The gauge-transformed right IF state is obtained by applying the gauge transformation, $\hat{G}$, to the bath, and its bath 1-RDM is transformed to Γ^G. **(d)** The impurity-bath time evolution operator, $\hat{U}_{SB}$, is approximated by an effective time evolution operator by projecting the bath to the effective bath orbitals after the gauge transformation, $\mathcal{P}_{m+1}\hat{G}_{m+1}\hat{U}^{SB}\hat{G}_m^{-1}\mathcal{P}_m$. The filled and unfilled rectangles represent the core and virtual orbital spaces and these spaces are projected into fully occupied and unoccupied states, respectively.

representation for the effective time evolution operator is illustrated in Fig. 4d.

The above tensor elements can be efficiently computed from determinant formulae. Since the configurations in the core and virtual orbitals are fixed, we can compute the determinant of block matrices, keeping the core and virtual orbital block matrices fixed. Therefore, the computational complexity to compute determinants for all configurations is $\mathcal{O}(N_b^3 + 2^{2N_{\text{eff}}}N_{\text{eff}}^3)$, where the first term corresponds to the computation of the determinant and inverse of the core and virtual orbital block matrices and the second term corresponds to the computation of the determinant of the effective bath orbital block matrices. The cost for computing the full set of MPS tensor elements at time-step N_t is $\mathcal{O}(N_b^3 N_t + 2^{2N_{\text{eff}}}N_{\text{eff}}^3 N_t)$, which is *linear* in the number of time-steps N_t.

III. CONTINUOUS-TIME FORMULATION OF IF-MPS

A. Boundary Influence functional tensor

Defining the continuous-time limit of the influence functional tensor network is in principle one way to eliminate the time-step error from the standard second-order Trotter decomposition, and in numerical applications allows for the introduction of a wide variety of higher-order differential integrators. However, as shown in [33], the IF-MPS shows a nonphysical entanglement entropy scaling in the limit of $\Delta t \to 0$, as the entanglement entropy always scales to zero. This suggests that the continuous-time limit requires a more careful treatment.

In particular, the formalism of continuous matrix product states (cMPS) [53, 54] describes a quantum wavefunction of continuous variables that (in general) supports a finite entanglement entropy as the discretization approaches the continuum limit. In this section, we show that the usual IF-MPS does not support a standard cMPS representation in the continuous-time limit, and instead a closely related object, the *boundary* influence functional MPS should be used. The boundary influence functional MPS is implicitly used in transverse contraction [26, 55] (e.g., Ref. [27] states that this becomes a continuous MPS in the continuum limit, without providing an explicit construction) and has previously been used in influence functional calculations with interacting baths [31].

Consider the continuous-time limit $\Delta t \to 0$, where $\hat{U}^{SB}$ can be expressed as,

$$\hat{U}^{SB} = \hat{I} - i(\hat{L}_{SB} + \hat{L}_B)\Delta t, \tag{31}$$

and the corresponding matrix elements of the IF-MPS, A^{s_i,s_f}, are,

$$\begin{aligned} A^{0,0} &= I - i\hat{L}_B\Delta t \\ A^{0,1} = A^{1,0} &= -i\hat{L}_{SB}\Delta t \\ A^{1,1} &= I - i\hat{L}_B\Delta t. \end{aligned} \tag{32}$$

These do not have the same form as the tensor entries in a cMPS [53, 54], which take the following form,

$$\begin{aligned} A^0 &= I + \epsilon Q \\ A^1 &= \sqrt{\epsilon} R \\ A^2 &= \frac{1}{2}\epsilon R^2, \end{aligned} \tag{33}$$

where Q and R are arbitrary matrices within the virtual bond space of the MPS, ϵ is the infinitesimal interval corresponding here to Δt on the temporal axis, and the upper indices 0, 1, and 2 label the number of excitations in the physical bond.

There are two main differences between Eq. 32 and Eq. 33. First, the IF has an additional 'I' term in $A^{1,1}$, that is not in A^2 in Eq. 33. Second, the A^1 terms are proportional to Δt, not $\sqrt{\Delta t}$. It is clear to see the effect of these two differences in the formulation of the differential equation of motion for the 1-RDM Γ^R. In the infinitesimal limit of Eq. 26, after expanding U^{SB} the first term becomes

$$\left[U^{SB}\Gamma^{R,m}U^{SB\dagger}\right]_B = \Gamma^{R,m} - i[L_B, \Gamma^{R,m}]\Delta t. \tag{34}$$

For the second term,

$$\left[U^{ASB}\Gamma^{\phi}U^{ASB\dagger}\right]_B = -\frac{1}{2}L_{SB}L_{SB}^{\dagger}\Delta t^2, \tag{35}$$

which vanishes at $\Delta t \to 0$. Therefore, the differential equation of motion for Γ^R becomes

$$\frac{d\Gamma^R}{dt} = -i[L_B, \Gamma^R]. \tag{36}$$

This corresponds to unitary dynamics in the super-Fock bath orbital space, which preserves the spectrum of Γ^R. The initial Γ^R is given by the pure state $|\rho_B\rangle\rangle$, so its single-particle spectrum consists of only 0 and 1. Thus, the entanglement entropy of the IF is zero. Note that this result is the manifestation of the fact that the term in Eq. 35 is proportional to $(\Delta t)^2$, instead of $(\Delta t)^1$, which implies that the bath dynamics does not have effective 'dissipation' terms.

To obtain a more proper continuum limit, we split $\hat{U}^{SB}$ into two parts. For clarity, we write $\hat{I}$ in Eq. 31 as $\hat{I}_S \otimes \hat{I}_B$. Similarly, $\hat{L}_B$ can also be written in product form, $\hat{I}_S \otimes \hat{L}_B$, and $\hat{L}_{SB}$ is the only term that acts on both the impurity and bath. We can split $\hat{L}_{SB}$ using its singular value decomposition,

$$\begin{aligned} \hat{L}_{SB} &= \sum_{s,i} t_{si}\hat{d}_s^{\dagger}\hat{a}_i + \text{h.c.} \\ &= \sum_{a=1}^{n_S} \hat{O}_a^S \otimes \hat{O}_a^B + \text{h.c.} \end{aligned} \tag{37}$$

$$\begin{aligned} t = USV &= (US^{1/2})(S^{1/2}V) = t^S t^B \\ \hat{O}_a^S = \sum_s t_{sa}^S \hat{d}_s^{\dagger}, &\quad \hat{O}_a^B = \sum_i t_{ai}^B \hat{a}_i, \end{aligned} \tag{38}$$

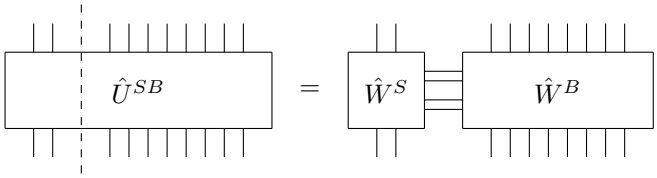

FIG. 5. The time evolution operator, $\hat{U}^{SB}$ can be split into two tensors, $\hat{W}^S$ and $\hat{W}^B$, which can be expressed as $\hat{U}^{SB} = \sum_a \hat{W}_a^S \otimes \hat{W}_a^B$. In the single impurity case with two impurity orbitals in the Liouville space, the index a has four components.

where n_S is the number of singular values. This leads us to write $\hat{U}^{SB}$ as follows,

$$\begin{aligned} \hat{U}^{SB} =&\ \hat{I}_S \otimes (\hat{I}_B - i\hat{L}_B\Delta t) \\ &+ \sum_{a=1}^{n_S} (\hat{O}_a^S\sqrt{\Delta t}) \otimes (-i\hat{O}_a^B\sqrt{\Delta t}) + \text{h.c.} \\ =&\ \sum_{a=0}^{2n_S} \hat{W}_a^S \otimes \hat{W}_a^B \end{aligned} \tag{39}$$

$$\begin{aligned} \hat{W}_a^S &= \begin{cases} \hat{I}_S & a = 0 \\ \hat{O}_a^S\sqrt{\Delta t} & 1 \le a \le n_S \\ \hat{O}_{a-n_S}^{S\dagger}\sqrt{\Delta t} & n_S + 1 \le a \le 2n_S \end{cases} \\ \hat{W}_a^B &= \begin{cases} \hat{I}_B - i\hat{L}_B\Delta t & a = 0 \\ -i\hat{O}_a^B\sqrt{\Delta t} & 1 \le a \le n_S \\ -i\hat{O}_{a-n_S}^{B\dagger}\sqrt{\Delta t} & n_S + 1 \le a \le 2n_S \end{cases} \end{aligned} \tag{40}$$

Therefore, instead of defining the elements of the MPS using $\hat{U}^{SB}$, we use $\hat{W}_a^B$. These are the tensor elements of the boundary IF-MPS. Its diagrammatic representation is drawn in Fig. 5. We can introduce a set of maximally entangled orbitals, $\hat{f}_a^{\dagger}$, on the auxiliary indices a thereby expressing $\hat{W}^B$ in a number-conserving format,

$$\hat{W}^B = \hat{I}_B - i\hat{L}_B\Delta t - i\sqrt{\Delta t}\sum_a \left(\hat{f}_a^{\dagger}\hat{O}_a^B + \text{h.c.}\right) \tag{41}$$

The matrix elements of the boundary IF-MPS are then given by,

$$\begin{aligned} W^{B,0} &= I_B - iL_B\Delta t \\ W^{B,1} &= -i\sqrt{\Delta t}\sum_a \left(f_a^{\dagger}O_a^B + \text{h.c.}\right) \\ W^{B,2} &= \Delta t\sum_a |\hat{O}_a^B|^2, \end{aligned} \tag{42}$$

which satisfies the form of Eq. 33 [56]. Therefore the boundary IF-MPS has a well-defined continuum limit. It is also possible to construct $\hat{W}^B$ from $\hat{U}^{SB}$ for general Δt outside the continuous-time limit, which is described in the Supplemental Material. Henceforth, we will implicitly assume that the IF-MPS refers to the boundary IF-MPS except where the distinction is important.

B. Gauge dynamics in the continuous-time IF-MPS

The boundary IF-MPS matrix elements define a new effective time evolution operator in the Liouville space of the system and bath with a well-defined continuous-time limit with non-vanishing entanglement entropy. This makes it possible to express and compress the MPS in the continuous-time limit.

As described in Sec. II D, in the case of a non-interacting bath, the object that defines the conversion to canonical form and the compression is the 1-RDM of the right/left IF state, Γ^R and Γ^L. Using $\hat{W}^B$, we can construct the corresponding iterative procedure to update the 1-RDM of the right/left IF state. In the continuous-time limit, $\Delta t \to 0$, this leads to an equation of motion for the 1-RDM of the right/left IF state.

The equation of motion for the 1-RDM of the right IF state, Γ^R, is given by,

$$\frac{d\Gamma^R}{dt} = t^{B\dagger}t^B - i[L_B, \Gamma^R] - \{t^{B\dagger}t^B, \Gamma^R\}, \tag{43}$$

where $\{A, B\} = AB + BA$ is an anti-commutator. A detailed derivation of this equation of motion is in the Supplemental Material. It clearly shows that t^B acts as a dissipation term. Similarly, the equation of motion for the 1-RDM of the left IF state, Γ^L, is given by,

$$\frac{d\Gamma^L}{dt} = t^{B\dagger}t^B + i[L_B, \Gamma^L] - \{t^{B\dagger}t^B, \Gamma^L\}. \tag{44}$$

From Γ^L, we can find the gauge transformation $\hat{G}$. This is then absorbed into the right IF state to canonicalize the IF-MPS. For Γ^G, the 1-RDM of the gauge-transformed right IF state, we first define the gauge-transformed time evolution operator

$$\begin{aligned}
\hat{W}^G &= \hat{G}\hat{W}^B\hat{G}^{-1} + \frac{d\hat{G}}{dt}\hat{G}^{-1}\Delta t = \\
&\hat{I}_B - i\hat{L}_{GB}\Delta t - i\sqrt{\Delta t}\sum_a \left(\hat{f}_a^\dagger \hat{F}_a^1 + \hat{F}_a^{2\dagger}\hat{f}_a\right), \\
\hat{L}_{GB} &= \hat{G}\hat{L}_B\hat{G}^{-1} + i\frac{d\hat{G}}{dt}\hat{G}^{-1}, \\
\hat{F}_a^1 &= \hat{G}\hat{O}_a^B\hat{G}^{-1} = \sum_i \kappa_{ai}^1 \hat{a}_i, \\
\kappa^1 &= t^B G^{-1}, \\
\hat{F}_a^{2\dagger} &= \hat{G}\hat{O}_a^{B\dagger}\hat{G}^{-1} = \sum_i \kappa_{ia}^2 \hat{a}_i^\dagger, \\
\kappa^2 &= G t^{B\dagger}.
\end{aligned} \tag{45}$$

Note that in the definition of $\hat{L}_{GB}$, we have taken $\Delta t \to 0$, and there is a term that takes into account the time dependence of the gauge transformation. The time derivative of the gauge transformation can be written as,

$$\begin{aligned}
\left[\frac{d\hat{G}}{dt}\hat{G}^{-1}\right]_{kl} &= \dot{g}_k g_k^{-1}\delta_{kl} - \sum_i g_k R_{ik}^{L*}\dot{R}_{il}^L g_l^{-1}, \\
\dot{g}_k g_k^{-1} &= \frac{1}{2\nu_k(1-\nu_k)}\dot{\nu}_k, \\
\dot{\nu}_k = -\left[R^{L\dagger}\dot{\Gamma}^L R^L\right]_{kk} &= -\sum_a |\sum_i t_{ai}^B R_{ik}^L|^2(1-2\nu_k), \\
\left[R^{L\dagger}\dot{R}^L\right]_{kl} &= -\frac{\left[R^{L\dagger}\dot{\Gamma}^L R^L\right]_{kl}}{\nu_l - \nu_k}\ (k \neq l) = \\
&\frac{1-\nu_k-\nu_l}{\nu_k-\nu_l}\left[R^{L\dagger}t^{B\dagger}t^B R^L\right]_{kl} + i\left[R^{L\dagger}L_B R^L\right]_{kl},
\end{aligned} \tag{46}$$

where we set the $\dot{R}^L$ terms to be zero when $k = l$ and $|\nu_k - \nu_l| < \varepsilon$. Note that R^L is only defined up to degenerate eigenvectors of Γ^L, therefore, to fix this redundancy, we propagate R^L with the regularized $\dot{R}^L$ from a reference time, which we set to be the final time of the Γ^L propagation.

With this gauge-transformed time evolution operator, the equation of motion for Γ^G can be written as follows.

$$\begin{aligned}
\frac{d\Gamma^G}{dt} &= \kappa^2\kappa^{2\dagger} - i(L_{GB}\Gamma^G - \Gamma^G L_{GB}^\dagger) - \{\kappa^2\kappa^{2\dagger}, \Gamma^G\} \\
&+ \Gamma^G\left[\kappa^2\kappa^{2\dagger} - \kappa^{1\dagger}\kappa^1 + i(L_{GB} - L_{GB}^\dagger)\right]\Gamma^G.
\end{aligned} \tag{47}$$

After obtaining Γ^G in this continuous-time picture, the effective bath orbitals and their rotation matrix, R^{eff} (see Sec. II D), can be defined from the eigenvectors of Γ^G. R^{eff} is then used to construct the time-dependent projection operator, $\mathcal{P}$, which defines the compression of the IF-MPS in the continuous-time setting.

C. Embedding Liouville operator for the embedded wavefunction

Once we solve the equation of motion for $\Gamma^G(t)$, its truncated spectrum defines a set of effective bath orbitals at all (continuous) times t. By projecting the original Liouville dynamics into the time-dependent embedding space (of system and bath orbitals) and retaining terms first order in Δt, we can extract the generator for the embedded wavefunction, which we call here the embedding Liouville operator, $\hat{L}^{\text{emb}}$. This yields a continuous-time state-vector propagation governed by the boundary IF-MPS.

First, by expanding Eq. 30, we have $\mathcal{P}\hat{L}_G\mathcal{P}$ where $\mathcal{P}$ is the projection operator into the effective bath orbitals and $\hat{L}_G = \hat{G}\hat{L}_{SB}\hat{G}^{-1} + \hat{L}_{GB}$. In addition, there is also a term for the time dependence of the effective bath orbitals in the projection operator. Using the rotation matrix of the effective bath orbitals, R^{eff}, the additional Liouville operator from this time dependence can be writ-

ten as,

$$\hat{X} = -i \sum_{m,n} \left[R^{\text{eff}\dagger} \dot{R}^{\text{eff}} \right]_{mn} \hat{a}_m^\dagger \hat{a}_n, \tag{48}$$

where m and n index the effective bath orbital basis. Finally, the impurity-only Liouville operator can be simply added. The embedding Liouville operator becomes,

$$\hat{L}^{\text{emb}} = \hat{L}_S + \mathcal{P}\hat{L}_G\mathcal{P} + \hat{X} = \hat{L}_S + \hat{L}_{SB}^{\text{emb}}. \tag{49}$$

We can now write down the equation of motion for the embedded wavefunction, $|\Psi^{\text{emb}}\rangle\rangle$, with which we can carry out state-vector propagation,

$$i\frac{d}{dt} |\Psi^{\text{emb}}\rangle\rangle = \hat{L}^{\text{emb}} |\Psi^{\text{emb}}\rangle\rangle . \tag{50}$$

Note that the embedding Liouville operator, $\hat{L}^{\text{emb}}$, is time-dependent.

D. Connections to embedding theories

We conclude this section by explicitly connecting to the formalism of real-time density matrix embedding theory (real-time DMET) [37, 47] and the closely related time-dependent complete-active-space self-consistent-field method (TD-CASSCF) [57, 58]. In particular, we focus on real-time DMET since the wavefunction ansatz in real-time DMET has the same form as the embedded wavefunction here [37],

$$|\Psi(t)\rangle = \sum_{s,b} \psi_{s,b}(t) |s\rangle \otimes |b\rangle = \sum_{s,b} \psi_{s,b}(t) |s,b\rangle , \tag{51}$$

where s and b are configurations in impurity and bath, respectively, and $\psi_{s,b}(t)$ are the corresponding time-dependent amplitudes. The selection of a finite number of effective bath orbitals limits possible bath configurations, and the effective bath orbitals are allowed to be time-dependent.

In the IF-MPS, the effective bath orbitals were determined by the bath 1-RDM. In contrast, in real-time DMET, the effective bath orbitals are determined by the time-dependent variational principle (TDVP), assuming the embedding wavefunction ansatz (51). The equation of motion from TDVP is

$$i\dot{\psi}_{s,b} = \langle s,b| \left(\hat{H} + \hat{X} \right) |\Psi\rangle , \tag{52}$$

$$|\dot{b}\rangle = i\hat{X} |b\rangle , \tag{53}$$

where $\hat{X}$ is a quadratic Hermitian operator that describes the time dependence of the effective bath orbitals, which has the same form as Eq. 48, but here, its elements are determined from the TDVP equations. The equation of motion in Eq. 52 defines the embedding Hamiltonian $\hat{H} + \hat{X}$ which corresponds to the embedding Liouville operator, $\hat{L}^{\text{emb}}$, in Eq. 49. Aside from the different generators of the bath dynamics, a qualitative difference between real-time DMET and the embedding scheme that derives from the IF-MPS in this work is the nonunitary nature of the gauge transformation, $\hat{G}$. In the real-time DMET, the $\hat{X}$ operator implements unitary dynamics of the effective bath orbitals.

IV. RESULTS

We now describe simulations that implement the above boundary IF-MPS formulation, including its continuous-time formulation, in the single impurity Anderson model. To generate reference results, we used state-vector propagation with a large bath discretization of the AIM. Specifically, we used $N_b = 40$ discrete bath orbitals (N_b refers to orbitals of each spin, i.e. 40 spin $\uparrow$ and 40 spin $\downarrow$ orbitals) to approximate the bath spectral density function, $J(\omega)$, using a linear scheme [3, 59], as follows

$$\begin{aligned} J(\omega) &= \frac{\Gamma}{\pi}\sqrt{1 - \frac{\omega^2}{W^2}}, \\ |t_i|^2 &= \int_{I_i} d\omega\, J(\omega), \\ E_i &= \frac{1}{|t_i|^2} \int_{I_i} d\omega\, \omega J(\omega), \end{aligned} \tag{54}$$

where $W = 10\Gamma$, $\omega \in [-W, W]$, and $I_i = [-W + \frac{2W}{N_b}(i-1), -W + \frac{2W}{N_b} i]$, and the impurity Hamiltonian parameters were chosen as $U = -2\varepsilon_\sigma = 2.5\pi\Gamma$. The initial bath state was taken to be the (decoupled) thermal state with $\Gamma\beta = 2$, and the impurity was quenched from an initial unoccupied state, $\hat{\rho}_S(0) = |0\rangle\langle 0|$. Benchmark results were then computed using the time-dependent density matrix renormalization group (tdDMRG) with bond dimension up to 600 using the Block2 [60, 61] package. We carried out a thermofield transformation on the bath orbitals to reduce the bond dimension of the MPS, as described in [5]. We then propagated the MPS using the two-site time-dependent variational principle. With the largest bond dimension 600 and a time-step size of $\Gamma\Delta t = 0.01$, all the local observables presented here are converged with respect to bond dimension and time-step to within an estimated absolute error of 10^{-5}.

The boundary IF-MPS calculations were carried out both in the standard discrete-time formulation as well as the continuous-time formulation of Secs. III B and III C. In the discrete-time case, we used the IF-MPS Slater determinant compression scheme applied to the boundary IF. The IF-MPS was constructed using both a second-order Trotter decomposition (Trotter2, Eq. 9) and a 4th-order Trotter decomposition (Trotter4) of the dynamics. The 4th-order Trotter decomposition is based on the

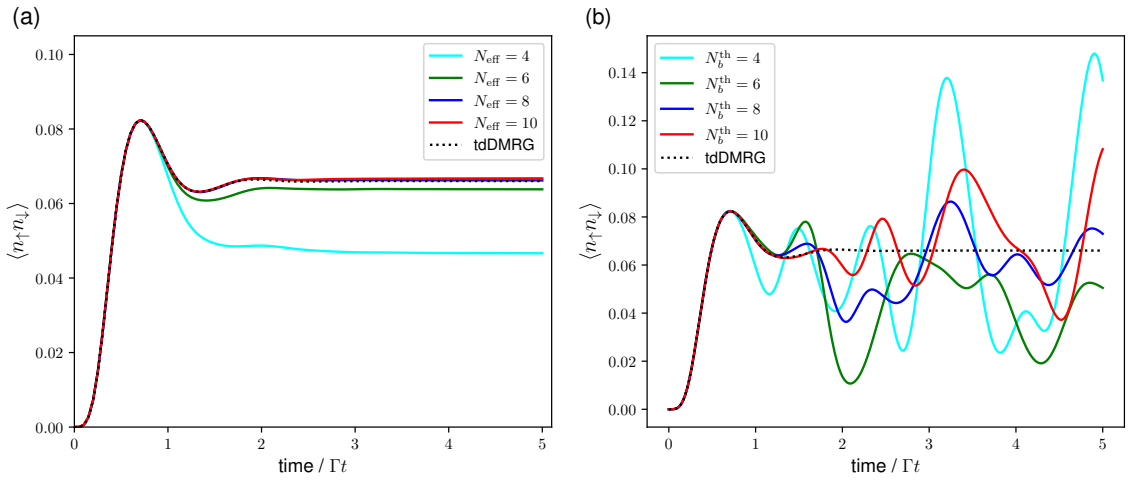

FIG. 6. The time-dependence of the double occupancy of the impurity, $\langle n_\uparrow n_\downarrow \rangle$, in the quench dynamics of the symmetric Anderson model with $U = 2.5\pi\Gamma$ and $\varepsilon_\sigma = -1.25\pi\Gamma$. The impurity is quenched from an initial unoccupied state and a thermal bath of temperature $\Gamma\beta = 2$. Reference results from time-dependent DMRG are shown (tdDMRG, black dotted). (a) Results from the discrete-time boundary IF-MPS using different numbers of effective bath orbitals, $N_{\text{eff}} = 4$ (cyan), 6 (green), 8 (blue), and 10 (red) with a time-step of $\Gamma\Delta t = 0.01$. This shows that at $N_{\text{eff}} = 8$ and 10, the IF-MPS dynamics are fully converged to the eye compared to the reference results. (b) Results from the time-independent Lanczos-based bath discretization with thermofield transformation using a series of static bath discretizations, $N_b^{\text{th}} = 4$ (cyan), 6 (green), 8 (blue), and 10 (red), where N_b^{th} is the number of Lanczos vectors in the thermofield transformed bath. The finite size bath errors are clearly larger than in (a).

Forest-Ruth formula [62, 63],

$$e^{-i\hat{L}\Delta t} \approx e^{-i\hat{L}_S\theta\Delta t/2}e^{-i\hat{L}_{SB}\theta\Delta t}e^{-i\hat{L}_S(1-\theta)\Delta t/2} e^{-i\hat{L}_{SB}(1-2\theta)\Delta t}e^{-i\hat{L}_S(1-\theta)\Delta t/2}e^{-i\hat{L}_{SB}\theta\Delta t}e^{-i\hat{L}_S\theta\Delta t/2}, \tag{55}$$

with the constant $\theta = 1/(2 - 2^{1/3})$ and a Trotter error of order $\mathcal{O}(\Delta t^5)$. Discrete-time boundary IF-MPS calculations were then performed for different numbers of effective bath orbitals N_{eff} of each spin, which formally corresponds to a boundary IF-MPS with a maximal bond dimension of $4^{N_{\text{eff}}}$. Note, however, that the system-bath coupling in the Anderson model does not couple up and down spins. Consequently, the IF-MPS factorizes into a spin-up and spin-down IF (each of maximal bond dimension $2^{N_{\text{eff}}}$) and we use this factorization for a more efficient implementation of the discrete-time boundary IF-MPS. The maximum bond dimension of $2^{N_{\text{eff}}}$ can be further reduced by only choosing the available configurations from the number-conserving $U(1)$ symmetry of the embedded wavefunction.

For the continuous-time implementation, we wrote the effective $\hat{L}^{\text{emb}}$ as a second-quantized fermionic operator which could then be used in state-vector propagation using a higher-order integrator such as 4th-order Runge-Kutta. Note that to apply 4th-order Runge-Kutta to the state-vector at time t, with time-step Δt, requires $\hat{L}^{\text{emb}}(t)$ at the intermediate time $t + \Delta t/2$. To obtain this, we propagated the bath 1-RDM equations of motion (Eqs. 43, 44) with a finer time-step Δt_{fine}, also with the 4th-order Runge-Kutta integrator. Since the cost to propagate the bath 1-RDM is much lower than that for the many-body wavefunction, we used Δt_{fine} much smaller than Δt to minimize the time-step error from the bath 1-RDM propagation. We fixed $\Gamma\Delta t_{\text{fine}} = 0.01/2^6 \approx 0.00016$ in this work. We then used the quantum chemistry full configuration interaction (exact diagonalization) implementation in PySCF [64, 65] to carry out the propagation of the state-vector.

One assumption for higher-order numerical propagators to be accurate is that the time-dependent embedding Liouville operator, $\hat{L}^{\text{emb}}$, is well-behaved, i.e. it does not change too sharply. However, in the initial and final periods of the time propagation, we observe that the spectrum of the Liouville operator diverges. This is because Γ^L consists of nearly core and virtual orbitals at either temporal boundary and large values of g_k and g_k^{-1} in the gauge transformation are applied to the effective bath orbital spaces.

This issue can easily be circumvented by initially propagating the wavefunction without the gauge transformation for a short time. In this short time period, the effective bath orbitals are taken from Γ^R and Γ^L. After the completion of this short time period, the gauge transformation is applied to the wavefunction, and subsequently, the wavefunction is propagated with the gauge-transformed equation of motion. We found that the spectrum of the Liouville operator showed instabilities up to an initial $\Gamma\Delta t_i = 0.06$ and after a final $\Gamma\Delta t_f = 0.1$ (Supplemental Material). We therefore used propagation

without gauges in these short periods, and between these boundary times, the wavefunction was propagated with the gauge transformation.

A. Effective bath orbitals versus bath discretization

As described in the analysis in Secs. II D, the IF-MPS time propagation can be viewed as propagating a wavefunction in the Liouville space of the impurity and a set of effective bath orbitals. We now compare this time-dependent discretization of the (Liouville) bath with a more standard time-independent discretization.

In Fig. 6, we show the time-dependence of the double occupancy of the impurity, $\langle n_\uparrow n_\downarrow \rangle$ in the quench dynamics. We show (second order Trotter discrete-time) IF-MPS dynamics generated using effective bath orbital numbers $N_{\text{eff}} = 4, 6, 8, 10$ with time-step $\Gamma\Delta t = 0.01$ (Fig. 6a). We also show results from a time-independent bath discretization scheme based on a Lanczos iteration with thermofield transformation [5, 66, 67]. The thermofield transformation transforms the initial thermal state with N_b bath orbitals to a Fermi sea with N_b filled orbitals and N_b empty orbitals and the Lanczos tridiagonalization algorithm over the filled and empty orbital space gives a truncated bath basis. We denote the number of Lanczos vectors in the truncated thermofield bath as N_b^{th}. We show dynamics using truncated thermofield bath discretizations with $N_b^{\text{th}} = 4, 6, 8, 10$ in Fig. 6b. The thermofield bath dynamics was propagated using the quantum chemistry full configuration interaction method and 4th-order Runge-Kutta with time-step $\Delta t = 0.005$.

As expected, the time-independent bath discretization yields substantial finite-size errors due to the limited number of Lanczos vectors supported by the bath, while the effective bath orbitals encode much more faithful dynamics. Indeed, at $N_{\text{eff}} = 8$, the dynamics is fully converged to the eye (the corresponding error from the reference DMRG dynamics is shown in the inset), while the $N_b^{\text{th}} = 10$ dynamics fails for $\Gamma t > 2$. This illustrates the compactness of the IF-MPS time-dependent bath description, which resembles the behavior seen in real-time quantum embedding studies [37] even though the bath dynamics in the current formulation is non-unitary.

B. Converging to the continuous-time limit

We now analyze the time-step error incurred by varying the time-step, $\Gamma\Delta t \in \{0.02/2^n | n = 0, 1, 2, \cdots, 6\}$, at three different propagated times, $\Gamma t = 2$, 3, and 5. The number of effective bath orbitals is fixed as $N_{\text{eff}} = 8$, which is well converged to the reference data as shown in the previous section. We examine the convergence by fitting to the function, $f(\Delta t) = A\Delta t^m + C$. The exponent m is extracted from the difference, $f(2\Delta t) - f(\Delta t) = A(2^m - 1)\Delta t^m \propto \Delta t^m$, without the knowledge of the constant term, C.

In Fig. 7, the differences in $\langle n_\uparrow n_\downarrow \rangle$, $|\langle n_\uparrow n_\downarrow \rangle(2\Delta t) - \langle n_\uparrow n_\downarrow \rangle(\Delta t)|$, are illustrated as a function of different time-steps, Δt. We compare four different boundary IF-MPS schemes to analyze the time-step errors - 1) discrete-time boundary IF-MPS with the second-order Trotter decomposition (Trotter2, Eq. 9), 2) discrete-time boundary IF-MPS with the 4th-order Trotter decomposition (Trotter4, Eq. IV), 3) continuous-time IF-MPS propagated by the 4th-order Runge-Kutta (RK4) method, and 4) continuous-time IF-MPS with the second-order Trotter decomposition (cont-Trotter2), which will be defined further below. The exponent m is extracted by fitting the differences at the four smallest time-steps, and the fitted function is plotted as dashed lines.

For all three different propagated times, the exponent for the RK4 method has 4th-order time-step errors, which agrees with the theoretical scaling. However, the exponent extracted from both the second-order and 4th-order Trotter decomposition in the discrete-time formulation shows that the error is first-order in time-step, despite the theoretical error scaling of each Trotter decomposition without tensor network compression. We further note that the extrapolations to the continuous-time limit ($\Delta t = 0$) from Trotter2 and RK4 agree with each other up to 10^{-6}, whereas the extrapolated results from the Trotter4 data do not (Supplemental Material). This is because the continuous-time limit of Trotter2 (for finite bond dimension) is the same as that of RK4, but that of Trotter4 is not because it involves time evolution in both the forward and backward time directions.

The above discrepancies in the time-step error scaling of the Trotter schemes imply that there is an additional first-order time-step error associated with the discrete-time tensor network compression. We can show that the first-order time-step error arises from the projection of the reference (i.e., $N_b = 40$) bath orbital space into the embedding space. For simplicity, we demonstrate this using a time-independent projection operator $\mathcal{P}$ without the gauge transformation and $\hat{L}_S = 0$,

$$\mathcal{P} e^{-i\hat{L}\Delta t}\mathcal{P}. \tag{56}$$

Expanding up to Δt^2, we obtain

$$\mathcal{P} - i\mathcal{P}\hat{L}\mathcal{P}\Delta t - \frac{1}{2}\mathcal{P}\hat{L}^2\mathcal{P}(\Delta t)^2 + \mathcal{O}((\Delta t)^3). \tag{57}$$

Now consider decreasing the time-step Δt to $\Delta t/2$. Then the time evolution operator for Δt can be written as

$$\mathcal{P} e^{-i\hat{L}\Delta t/2}\mathcal{P} e^{-i\hat{L}\Delta t/2}\mathcal{P}, \tag{58}$$

and by expanding it up to Δt^2, we find

$$\mathcal{P} - i\mathcal{P}\hat{L}\mathcal{P}\Delta t - \frac{1}{4}\left(\mathcal{P}\hat{L}^2\mathcal{P} + \mathcal{P}\hat{L}\mathcal{P}\hat{L}\mathcal{P}\right)(\Delta t)^2 + \mathcal{O}((\Delta t)^3) \tag{59}$$

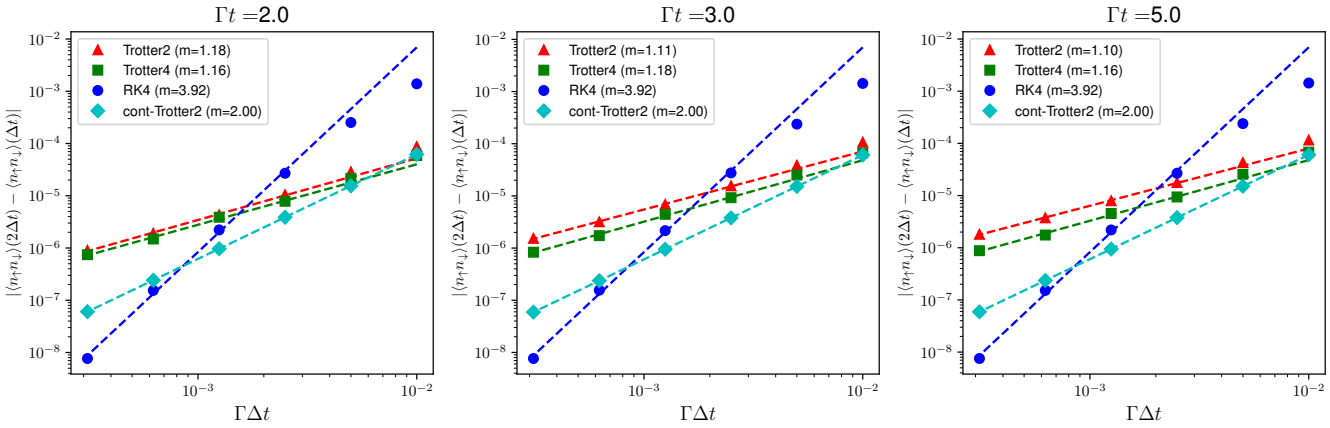

FIG. 7. The difference in double occupancy $\langle n_\uparrow n_\downarrow\rangle$ between two different time-steps, Δt and $2\Delta t$ using discrete-time IF-MPS with the second- and 4th-order Trotter decomposition (labeled as Trotter2 and Trotter4 with red triangles and green squares, respectively) and continuous-time IF-MPS with the 4th order Runge Kutta method and the second-order Trotter decomposition (labeled as RK4 and cont-Trotter2 with blue circles and cyan diamonds, respectively) at propagated times, $\Gamma t = 2, 3$, and 5, with the number of effective bath orbitals, $N_{\text{eff}} = 8$. The results are fitted by the function, $\log|\langle n_\uparrow n_\downarrow\rangle(2\Delta t) - \langle n_\uparrow n_\downarrow\rangle(\Delta t)| = m\log\Delta t + b$, and the fits are displayed with dashed lines.

The two expressions agree to first-order in the time-step, but not to second-order in the time-step, due to the difference between $\mathcal{P}\hat{L}^2\mathcal{P}$ and $(\mathcal{P}\hat{L}\mathcal{P})^2$. Thus, after summing over $t/\Delta t$ time-steps, the total propagation has first-order time-step error, $\mathcal{O}(\Delta t)$. The IF-MPS compression involves time-dependent projection operators $\mathcal{P}(t)$ together with gauge transformations $\hat{G}(t)$. However, by assuming the smoothness of $\mathcal{P}(t)$ and $\hat{G}(t)$ in time, it is easy to show that the discrete-time IF-MPS also has this first-order time-step error.

Based on the above analysis, we can consider a modified Trotter decomposition method that is obtained from the continuous boundary IF-MPS. We denote this as the cont-Trotter method to distinguish it from the previous Trotter methods. To obtain the cont-Trotter decomposition, we make the replacement,

$$\mathcal{P}e^{-i\hat{L}\Delta t}\mathcal{P} \to \mathcal{T}e^{-i\int \mathcal{P}\hat{L}\mathcal{P}dt} = \mathcal{T}e^{-i\int \hat{L}^{\text{emb}}_{SB}dt}, \qquad (60)$$

where the integration is over the time-step interval Δt and $\mathcal{T}$ refers to a fermionic time-ordering operator. This can also be interpreted as a generalized time-dependent Trotter decomposition [68] of the embedding Liouville operator. The time-ordered operator can be expressed using the following differential equation,

$$\hat{U}(x) = \mathcal{T}e^{-i\int_{t_i}^{t_i+x}\hat{L}^{\text{emb}}_{SB}dt},$$
$$\frac{d}{dx}\hat{U}(x) = -i\hat{L}^{\text{emb}}_{SB}(t_i+x)\,\hat{U}(x), \qquad (61)$$

and the desired operator is $\hat{U}(\Delta t)$. Since $\hat{L}^{\text{emb}}_{SB}$ is a non-interacting operator, solving this differential equation of motion for $\hat{U}(x)$ is efficient (noting that the time evolution operator at $x = 0$ is given by the identity operator, $\hat{U}(0) = \hat{I}$). We solve the differential equation using 4th-order Runge Kutta with time-step $2\Delta t_{\text{fine}}$, which allows us to include all the time-information of $\hat{L}^{\text{emb}}_{SB}$ obtained from the bath 1-RDM propagation with a Δt_{fine} time-step.

In Fig. 7, time-step errors from the second-order cont-Trotter decomposition of the continuous-time IF-MPS clearly show that this gives second-order time-step errors. Indeed, the time-step propagation error with this technique is better even than that of 4th-order Runge-Kutta except for very small time-steps.

V. CONCLUSIONS

In this work, by analyzing the tensor network influence functional (IF-MPS) for the Anderson impurity model, we derived the correct continuous-time limit via the boundary IF-MPS. We further established a correspondence to discretized bath dynamics and quantum embedding. These formal results clarify the connection between the IF-MPS and other long-standing numerical techniques. They also provide the foundation to develop improved numerical implementations, for example, through the higher-order propagators identified in this work.

The numerical results we obtained on the quench dynamics of the Anderson model demonstrate the advantages of the current formulation. For example, compared to discrete-time IF-MPS, by using the equations of motion we derive, we can obtain high-order convergence of the time-step error. This is in contrast to increasing the order of the Trotterization in the standard discrete time approach, which does not in fact improve the time-step convergence, due to the errors associated with compression.

Our results also support the advantages of IF-MPS dy-

namics in a more general sense: through defining, implicitly, a time-dependent bath representation, we find we achieve a much more compact description of the influence of the bath than prior static bath discretizations.

The connections between IF-MPS and standard state-vector propagation further open up the application of a wide variety of wavefunction-based simulation tools within the boundary IF-MPS framework. We plan to explore the potential of these developments in a variety of physical applications in future work.

VI. ACKNOWLEDGEMENTS

This material is based upon work supported by the U.S. Department of Energy, Office of Science, Office of Advanced Scientific Computing Research and Office of Basic Energy Sciences, Scientific Discovery through Advanced Computing (SciDAC) program under Award Number DE-SC0022088.

[1] S. Paeckel, T. Köhler, A. Swoboda, S. R. Manmana, U. Schollwöck, and C. Hubig, Annals of Physics **411**, 167998 (2019).
[2] F. Heidrich-Meisner, A. E. Feiguin, and E. Dagotto, Phys. Rev. B **79**, 235336 (2009).
[3] F. A. Wolf, I. P. McCulloch, and U. Schollwöck, Phys. Rev. B **90**, 235131 (2014).
[4] M. Ganahl, M. Aichhorn, H. G. Evertz, P. Thunström, K. Held, and F. Verstraete, Phys. Rev. B **92**, 155132 (2015).
[5] L. Kohn and G. E. Santoro, Journal of Statistical Mechanics: Theory and Experiment **2022**, 063102 (2022).
[6] L. Mühlbacher and E. Rabani, Physical Review Letters **100**, 10.1103/physrevlett.100.176403 (2008).
[7] G. Cohen and E. Rabani, Phys. Rev. B **84**, 075150 (2011).
[8] E. Gull, A. J. Millis, A. I. Lichtenstein, A. N. Rubtsov, M. Troyer, and P. Werner, Reviews of Modern Physics **83**, 349 (2011).
[9] E. Gull, D. R. Reichman, and A. J. Millis, Physical Review B **82**, 10.1103/physrevb.82.075109 (2010).
[10] G. Cohen, E. Gull, D. R. Reichman, A. J. Millis, and E. Rabani, Phys. Rev. B **87**, 195108 (2013).
[11] G. Cohen, E. Gull, D. R. Reichman, and A. J. Millis, Phys. Rev. Lett. **112**, 146802 (2014).
[12] G. Cohen, D. R. Reichman, A. J. Millis, and E. Gull, Physical Review B **89**, 10.1103/physrevb.89.115139 (2014).
[13] R. Feynman and F. Vernon, Annals of Physics **281**, 547 (2000).
[14] Y. Tanimura and R. Kubo, Journal of the Physical Society of Japan **58**, 101 (1989).
[15] J. Jin, X. Zheng, and Y. Yan, The Journal of Chemical Physics **128**, 10.1063/1.2938087 (2008), 234703.
[16] D. Hou, R. Wang, X. Zheng, N. Tong, J. Wei, and Y. Yan, Phys. Rev. B **90**, 045141 (2014).
[17] E. Arrigoni, M. Knap, and W. von der Linden, Phys. Rev. Lett. **110**, 086403 (2013).
[18] A. Dorda, M. Nuss, W. von der Linden, and E. Arrigoni, Phys. Rev. B **89**, 165105 (2014).
[19] A. Dorda, M. Ganahl, H. G. Evertz, W. von der Linden, and E. Arrigoni, Phys. Rev. B **92**, 125145 (2015).
[20] F. Chen, G. Cohen, and M. Galperin, Phys. Rev. Lett. **122**, 186803 (2019).
[21] F. Chen, E. Arrigoni, and M. Galperin, New Journal of Physics **21**, 123035 (2019).
[22] N. Makri, Chemical Physics Letters **193**, 435 (1992).
[23] N. Makri and D. E. Makarov, The Journal of Chemical Physics **102**, 4600 (1995).
[24] S. Weiss, J. Eckel, M. Thorwart, and R. Egger, Phys. Rev. B **77**, 195316 (2008).
[25] D. Segal, A. J. Millis, and D. R. Reichman, Phys. Rev. B **82**, 205323 (2010).
[26] M. C. Bañuls, M. B. Hastings, F. Verstraete, and J. I. Cirac, Phys. Rev. Lett. **102**, 240603 (2009).
[27] M. B. Hastings and R. Mahajan, Phys. Rev. A **91**, 032306 (2015).
[28] A. Strathearn, P. Kirton, D. Kilda, J. Keeling, and B. W. Lovett, Nature Communications **9**, 10.1038/s41467-018-05617-3 (2018).
[29] M. Cygorek, M. Cosacchi, A. Vagov, V. M. Axt, B. W. Lovett, J. Keeling, and E. M. Gauger, Nature Physics **18**, 662 (2022).
[30] D. Gribben, D. M. Rouse, J. Iles-Smith, A. Strathearn, H. Maguire, P. Kirton, A. Nazir, E. M. Gauger, and B. W. Lovett, PRX Quantum **3**, 010321 (2022).
[31] E. Ye and G. K.-L. Chan, The Journal of Chemical Physics **155**, 044104 (2021).
[32] M. R. Jørgensen and F. A. Pollock, Phys. Rev. Lett. **123**, 240602 (2019).
[33] M. Sonner, A. Lerose, and D. A. Abanin, Annals of Physics **435**, 168677 (2021), special issue on Philip W. Anderson.
[34] J. Thoenniss, A. Lerose, and D. A. Abanin, Phys. Rev. B **107**, 195101 (2023).
[35] N. Ng, G. Park, A. J. Millis, G. K.-L. Chan, and D. R. Reichman, Phys. Rev. B **107**, 125103 (2023).
[36] J. Thoenniss, M. Sonner, A. Lerose, and D. A. Abanin, Phys. Rev. B **107**, L201115 (2023).
[37] J. S. Kretchmer and G. K.-L. Chan, The Journal of Chemical Physics **148**, 054108 (2018).
[38] M. Schmutz, Zeitschrift für Physik B Condensed Matter **30**, 97 (1978).
[39] A. A. Dzhioev and D. S. Kosov, The Journal of Chemical Physics **134**, 10.1063/1.3548065 (2011), 044121.
[40] U. Harbola and S. Mukamel, Physics Reports **465**, 191 (2008).
[41] T. Prosen, New Journal of Physics **10**, 043026 (2008).
[42] M. T. Fishman and S. R. White, Phys. Rev. B **92**, 075132 (2015).
[43] G. Petrica, B.-X. Zheng, G. K.-L. Chan, and B. K. Clark, Phys. Rev. B **103**, 125161 (2021).
[44] U. Schollwöck, Annals of Physics **326**, 96 (2011).
[45] G. Knizia and G. K.-L. Chan, Physical Review Letters **109**, 10.1103/physrevlett.109.186404 (2012).

[46] S. Wouters, C. A. Jiménez-Hoyos, Q. Sun, and G. K.-L. Chan, Journal of Chemical Theory and Computation **12**, 2706 (2016), pMID: 27159268, https://doi.org/10.1021/acs.jctc.6b00316.

[47] D. Yehorova and J. S. Kretchmer, The Journal of Chemical Physics **158**, 10.1063/5.0146973 (2023), 131102.

[48] I. Peschel, Brazilian Journal of Physics **42**, 267 (2012).

[49] H.-K. Jin, R.-Y. Sun, Y. Zhou, and H.-H. Tu, Phys. Rev. B **105**, L081101 (2022).

[50] N. Schuch and B. Bauer, Phys. Rev. B **100**, 245121 (2019).

[51] U. Manthe, H. Meyer, and L. S. Cederbaum, The Journal of Chemical Physics **97**, 3199 (1992).

[52] H.-D. Meyer, U. Manthe, and L. Cederbaum, Chemical Physics Letters **165**, 73 (1990).

[53] F. Verstraete and J. I. Cirac, Phys. Rev. Lett. **104**, 190405 (2010).

[54] M. Ganahl, J. Rincón, and G. Vidal, Phys. Rev. Lett. **118**, 220402 (2017).

[55] B. Pirvu, V. Murg, J. I. Cirac, and F. Verstraete, New Journal of Physics **12**, 025012 (2010).

[56] The factor of 1/2 difference from $W^{B,2}$ comes from the fact that Eq. 33 describes double excitations of indistinguishable bosonic particles whereas $W^{B,2}$ takes into account different auxiliary fermions.

[57] T. Sato and K. L. Ishikawa, Phys. Rev. A **88**, 023402 (2013).

[58] R. P. Miranda, A. J. Fisher, L. Stella, and A. P. Horsfield, The Journal of Chemical Physics **134**, 244101 (2011).

[59] I. de Vega, U. Schollwöck, and F. A. Wolf, Phys. Rev. B **92**, 155126 (2015).

[60] H. Zhai and G. K.-L. Chan, The Journal of Chemical Physics **154**, 10.1063/5.0050902 (2021), 224116.

[61] H. Zhai, H. R. Larsson, S. Lee, Z.-H. Cui, T. Zhu, C. Sun, L. Peng, R. Peng, K. Liao, J. Tölle, J. Yang, S. Li, and G. K.-L. Chan, The Journal of Chemical Physics **159**, 234801 (2023), https://pubs.aip.org/aip/jcp/article-pdf/doi/10.1063/5.0180424/18264237/234801_1_5.0180424.pdf.

[62] E. Forest and R. D. Ruth, Physica D: Nonlinear Phenomena **43**, 105 (1990).

[63] J. J. García-Ripoll, New Journal of Physics **8**, 305 (2006).

[64] Q. Sun, T. C. Berkelbach, N. S. Blunt, G. H. Booth, S. Guo, Z. Li, J. Liu, J. D. McClain, E. R. Sayfutyarova, S. Sharma, *et al.*, Wiley Interdisciplinary Reviews: Computational Molecular Science **8**, e1340 (2018).

[65] Q. Sun, X. Zhang, S. Banerjee, P. Bao, M. Barbry, N. S. Blunt, N. A. Bogdanov, G. H. Booth, J. Chen, Z.-H. Cui, *et al.*, The Journal of chemical physics **153** (2020).

[66] I. de Vega and M.-C. Bañuls, Phys. Rev. A **92**, 052116 (2015).

[67] A. Nüßeler, I. Dhand, S. F. Huelga, and M. B. Plenio, Phys. Rev. B **101**, 155134 (2020).

[68] J. Huyghebaert and H. D. Raedt, Journal of Physics A: Mathematical and General **23**, 5777 (1990).

Supplemental Material for "Tensor network influence functionals in the continuous-time limit: connections to quantum embedding, bath discretization, and higher-order time propagation"

SM-I. ADDITIONAL DATA

A. Diagonal elements of impurity reduced density operator

In the main text, we showed the time-dependence of the double occupancy, $\langle n_\uparrow n_\downarrow \rangle$, following a quench dynamics of the symmetric Anderson model with $U = 2.5\pi\Gamma$ and $\varepsilon_\sigma = -1.25\pi\Gamma$ from the initially unoccupied impurity state and a thermal bath of temperature $\Gamma\beta = 2$. In this section, we present additional data for diagonal elements of the impurity reduced density operator, $p_{\alpha\beta}(t) = \langle \alpha\beta | \, \hat{\rho}_S(t) \, | \alpha\beta \rangle$, where $\alpha, \beta \in \{0, 1\}$ is the configuration of spin $\uparrow$ and $\downarrow$. For example, the double occupancy can be expressed as $\langle n_\uparrow n_\downarrow \rangle = p_{11}$. In Fig. S1, we compare results from the discrete-time formulation of the boundary IF with $N_{\text{eff}} = 8$ effective bath orbitals to the benchmark result from time-dependent DMRG (tdDMRG) with bond-dimension 600, as explained in the main text. The density operator elements are normalized so the trace is 1, $\operatorname{Tr} \hat{\rho}_S(t) = 1$. The maximum errors are of the order of 10^{-3} in the intermediate regime ($\Gamma t \approx 2.0$) and the errors at the steady state limit ($\Gamma t \gtrsim 3.0$) are of the order of 10^{-4}, compared to the results from tdDMRG.

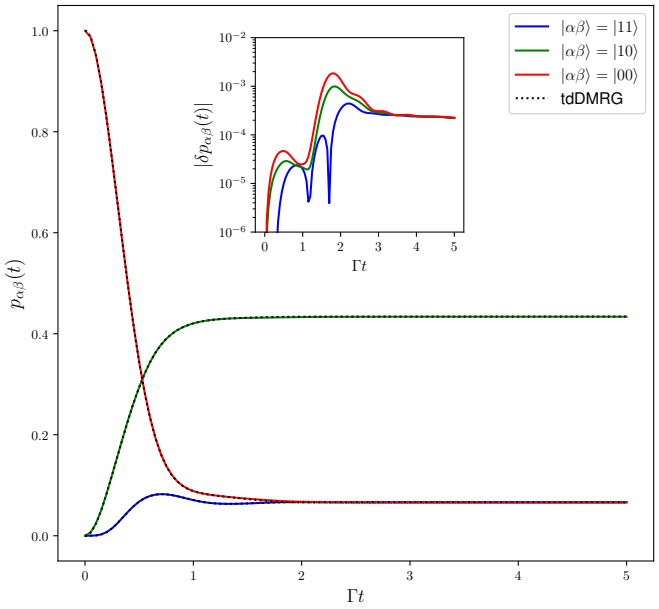

FIG. S1. Diagonal elements of the impurity reduced density operator $p_{\alpha\beta}(t) = \langle \alpha\beta | \, \hat{\rho}_S(t) \, | \alpha\beta \rangle$ of the symmetric Anderson model with $U = 2.5\pi\Gamma$ and $\varepsilon_\sigma = -1.25\pi\Gamma$. The impurity is quenched from an unoccupied initial state with a thermal bath at temperature $\Gamma\beta = 2$. Dotted lines are results from time-dependent DMRG (tdDMRG) with a bond-dimension 600 and solid lines are results from the discrete-time boundary IF-MPS with a number of effective bath orbitals $N_{\text{eff}} = 8$ and a timestep of $\Gamma\Delta t = 0.01$. **(inset)** Absolute deviations in $p_{\alpha\beta}(t)$ compared to the results of tdDMRG.

B. Spectrum of embedding Liouville operator

In this section, we show the instabilities of the embedding Liouville operator, $\hat{L}^{\text{emb}}$, close to the boundary times. Fig. S2 shows the 4 largest eigenvalues of $\hat{L}^{\text{emb}}$ constructed from the boundary IF with total propagated time, $\Gamma t = 2$.

The spectrum shows the instabilities at the initial and final boundary times, which are denoted by dashed lines at $\Gamma\Delta t_i = 0.06$ and $\Gamma\Delta t_f = 0.1$. We observe similar instabilities for other total propagation times up to $\Gamma t = 5$.

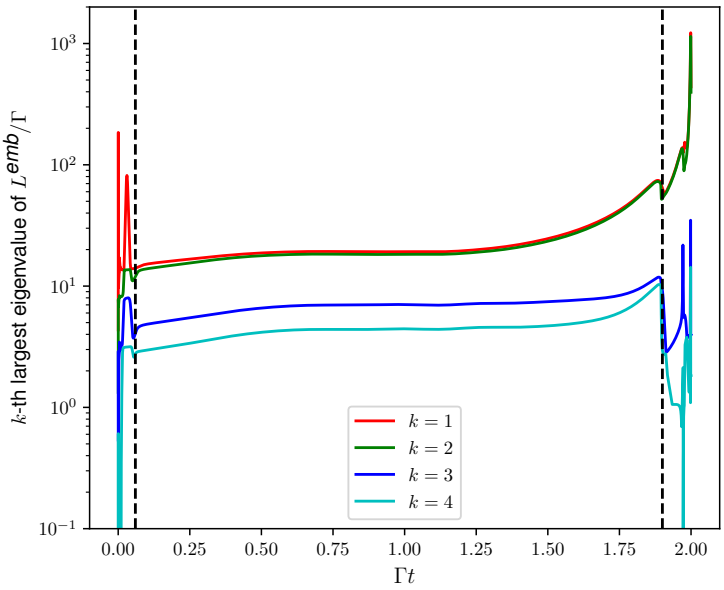

FIG. S2. The 4 largest eigenvalues of the embedding Liouville operator, $\hat{L}^{\text{emb}}$, constructed from the IF with the total propagated time, $\Gamma t = 2$. The spectrum shows the instabilities at the initial and final boundary times, which are denoted by dashed lines at $\Gamma\Delta t_i = 0.06$ and $\Gamma\Delta t_f = 0.1$.

C. Temporal Entanglement Entropy of Boundary IF

In Ref. [S33], the authors reported the vanishing temporal entanglement entropy scaling in the continuous-time limit from the Hamiltonian dynamics of the one-dimensional spin chain, and [S35] shows that this scaling also holds for SIAM. We showed that the equation of motion constructed in the continuous-time limit leads to unitary dynamics in the super-Fock bath orbital space, which preserves the spectrum of the 1-RDM, and hence the spectrum consists of only 0 and 1 with zero entanglement entropy of the IF.

The boundary IF was proposed in the main text to modify the behavior of the IF to yield a meaningful continuous-time limit. The tensor elements satisfy the form of a continuous-matrix product state and hence its physical properties including the entanglement entropy are well-defined as the discretization is changed. In Fig. S3, we numerically demonstrate that the temporal entanglement entropy is almost invariant to the time discretization. The entanglement entropy of the boundary IF is increasing very slowly over the propagated time, which allows us to achieve an efficient classical simulation in the long-time limit.

D. Temporal Entanglement Entropy of one-dimensional Ising model

As shown in the above section, the entanglement entropy of the IF depends on the boundary splitting. In this section, we show that the above boundary splitting also allows for a temporal entanglement entropy that converges to a nontrivial value as a function of timestep size in the one-dimensional Ising model (which represents IF dynamics with a non-quadratic interacting bath). Fig. S4 shows data from two different splitting schemes of the time-evolution operators, the first one absorbs singular values to the boundary, which corresponds to the ordinary influence functional in [S33], and the second one splits the singular values, which corresponds to the boundary influence functional.

In this section, we denote this difference as a boundary 'gauge', or simply gauge for short, where we call the first gauge the 'absorb' gauge and the second, the 'split' gauge. However, we stress that the gauge term here is different from the 'gauge' in the main text, where the gauge referred to the gauge structure along the temporal direction. We

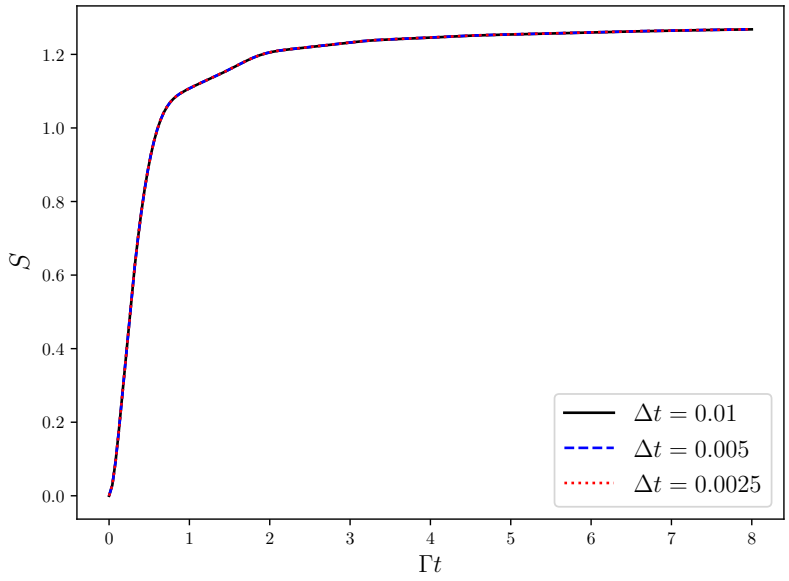

FIG. S3. Temporal entanglement entropy of the boundary influence functional at the half-cut with three different timesteps, $\Gamma\Delta t = 0.01, 0.005$, and 0.0025, as a function of total propagated time. The other parameters are set to be the same as the main text. The figure clearly shows that the values of entanglement entropy from three different timesteps overlap each other.

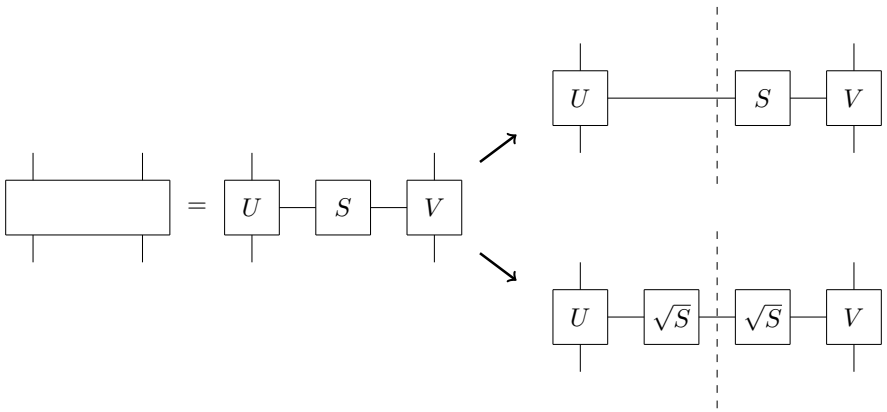

FIG. S4. Influence functional tensors can be constructed from gates after splitting the gate with a singular value decomposition. The singular values can be either absorbed to the influence functional tensors (right upper side, we denote this the 'absorb' gauge) or split to both sides (right lower side, we denote this the 'split' gauge).

demonstrate the effect of the boundary gauge on the temporal entanglement entropy for a one-dimensional quantum Ising chain with both transverse and longitudinal magnetic fields,

$$H = -\sum_i (J\sigma_i^z\sigma_{i+1}^z + g\sigma_i^x + h\sigma_i^z), \tag{S1}$$

initialized in a polarized product state, $|Z+\rangle = \lim_{N\to\infty} |0\rangle^{\otimes N}$. We fix $J = 1$ and tune the other two parameters to test both integrable ($g = 0.5$, $h = 0.0$) and nonintegrable ($g = -1.05$, $h = 0.5$) systems with three different timesteps, $\Delta t = 0.01$, 0.02, and 0.04. We use second-order Trotter decomposition to represent the time-evolution operators.

Fig. S5 shows the temporal entanglement entropy as a function of propagated time in integrable and nonintegrable models for three different timesteps with two different boundary gauges. The values of the temporal entanglement entropy are converged with respect to the bond dimensions and the singular value cutoffs. It clearly shows that the absorb gauge leads to zero temporal entanglement entropy as the timestep goes to zero, which agrees with [S33], whereas the split boundary gauge allows us to get an almost timestep-invariant temporal entanglement entropy that avoids the zero temporal entanglement entropy behavior for both integrable and nonintegrable models. This shows

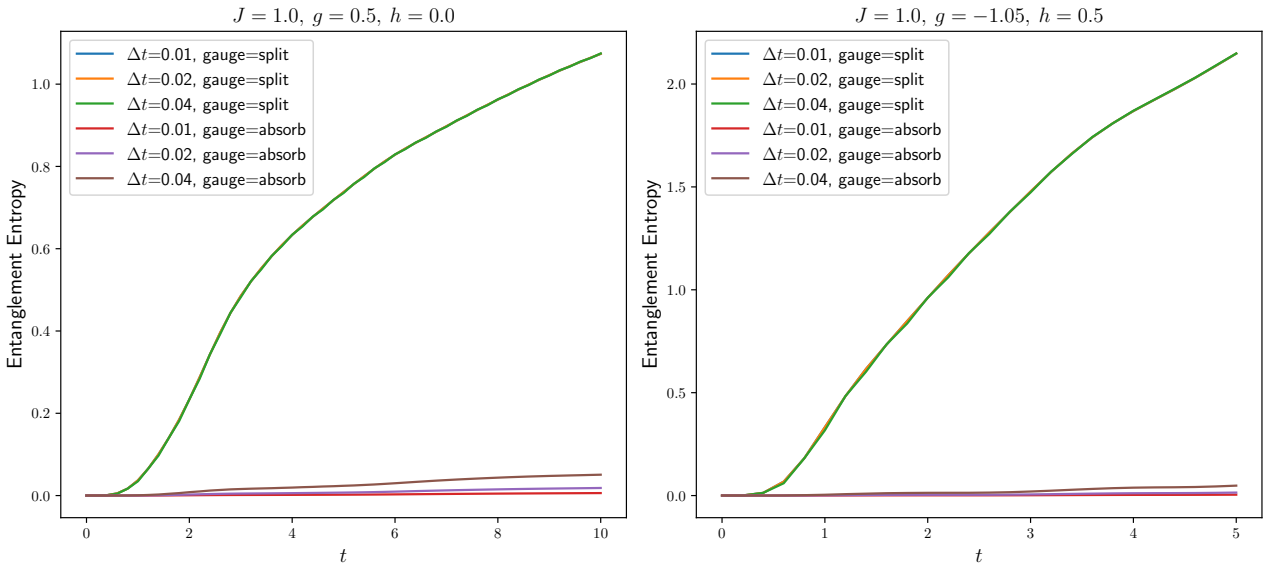

FIG. S5. Temporal Entanglement entropy from the quench dynamics of the quantum Ising model with both transverse and longitudinal magnetic field, with a polarized initial state, $|Z+\rangle = \lim_{N\to\infty} |0\rangle^{\otimes N}$. We consider two sets of parameters for the Hamiltonian, one correspond to an integrable system, $J = 1.0$, $g = 0.5$, $h = 0.0$ (left), and the other to a nonintegrable system, $J = 1.0$, $g = -1.05$, $h = 0.5$ (right) with three different timesteps, $\Delta t = 0.01$, 0.02, and 0.04 with two different boundary gauges. It clearly shows that the absorb gauge leads to zero temporal entanglement entropy as the timestep goes to zero whereas the split boundary gauge allows us to get an almost timestep-invariant temporal entanglement entropy with a non-trivial temporal entanglement entropy in the continuous time limit for both integrable and nonintegrable models.

that the boundary influence functional with the split gauge contains the correct continuous-time limit and that its entanglement entropy properly reflects the complexity of the classical simulation without timestep dependence. Additionally, it avoids the numerical instabilities associated with small singular values which appear in the absorb gauge due to the zero entanglement entropy when using small timesteps.

E. Timestep extrapolated data

In this section, we report the values of double occupancy compared to the results of tdDMRG after the zero-timestep extrapolation for four different methods described in the main text with three different propagated times (Fig. S6). These results show that the extrapolated dynamics from the discrete-time IF-MPS and the continuous-time IF-MPS are consistent, as the difference between the results from Trotter2, RK4, and cont-Trotter2 lies within 10^{-5}.

However, the results from Trotter4 have different errors in comparison to the other three methods. This is because the discrete-time IF-MPS from Trotter2 and the continuous-time IF-MPS converge to the same object in the continuous-time limit but the discrete-time IF-MPS from Trotter4 does not since it involves time evolution both in the forward and backward time direction.

SM-II. SUPER-FERMION REPRESENTATION

In this section, we describe the super-fermion representation in more detail. The super-fermion representation vectorizes the density operator, $\hat{\rho}$, giving a wavefunction in a Liouville space, $|\rho\rangle\!\rangle$. For brevity, spin indices will be omitted unless necessary. The Liouville space forms a super-Fock space with twice the number of orbitals. Formally, it can be found by applying the density operator to a 'left vacuum' state, $|I\rangle\!\rangle$, $|\rho\rangle\!\rangle = \hat{\rho}\,|I\rangle\!\rangle$,

$$|I\rangle\!\rangle = \prod_i (c_i^\dagger + \tilde{c}_i^\dagger)\,|0\rangle\!\rangle = \exp\left(\sum_i c_i^\dagger \tilde{c}_i\right)|\mathbf{0}\rangle \otimes |\mathbf{1}\rangle\,, \tag{S2}$$

where the empty orbitals, $|\mathbf{0}\rangle$, are from the original Fock space, and the fully occupied orbitals, $|\mathbf{1}\rangle$, are from the extended Fock space. The application of $\hat{\rho}$ into $|I\rangle\!\rangle$ can be interpreted as a particle-hole transformation of the bra

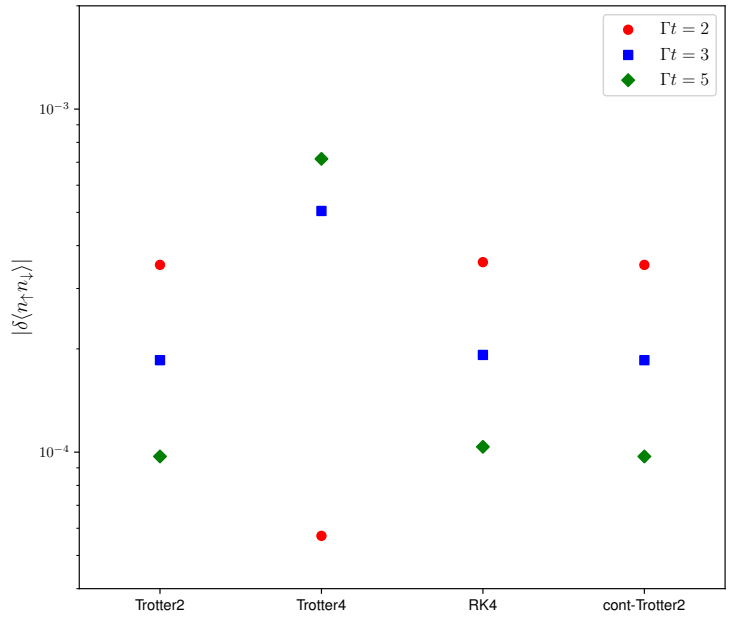

FIG. S6. The values of the double occupancy compared to the results of tdDMRG after the extrapolation of the timestep to zero for the four different methods described in the main text with the three different propagated times. The difference between the results from Trotter2, RK4, and cont-Trotter2 is within 10^{-5} whereas the results from Trotter4 extrapolate to a different limit compared to the other three methods.

of the density operator, and $|I\rangle\rangle$ can be interpreted as a set of fermionic Bell pairs. It is easy to see the following relation,

$$c_i |I\rangle\rangle = \tilde{c}_i |I\rangle\rangle , \quad c_i^\dagger |I\rangle\rangle = -\tilde{c}_i^\dagger |I\rangle\rangle . \tag{S3}$$

For example, for the thermal initial bath, $\hat{\rho}_B$, with an inverse temperature, β,

$$\hat{\rho}_B = \left(\frac{1}{1+e^{-\beta E_i}} |0\rangle\langle 0| + \frac{e^{-\beta E_i}}{1+e^{-\beta E_i}} |1\rangle\langle 1| \right)^{\otimes N_b} = \left(f_-(E_i,\beta) |0\rangle\langle 0| + f_+(E_i,\beta) |1\rangle\langle 1| \right)^{\otimes N_b} , \tag{S4}$$

the super-fermion representation, $|\rho_B\rangle\rangle$, is

$$|\rho_B\rangle\rangle = \prod_i \left(f_+(E_i,\beta)\hat{c}_i^\dagger + f_-(E_i,\beta)\hat{\tilde{c}}_i^\dagger \right) |0\rangle\rangle . \tag{S5}$$

The expectation value for an observable $\hat{O}$ is given by,

$$\mathrm{Tr}\left[\hat{O}\hat{\rho}\right] = \langle\langle I| \hat{O} |\rho\rangle\rangle . \tag{S6}$$

Therefore, $|\mathrm{Tr}_B\rangle\rangle$ in the main text has the same expression as $|I\rangle\rangle$. From the von Neumann equation,

$$i\frac{d}{dt}\hat{\rho} = [\hat{H},\hat{\rho}] = \hat{H}\hat{\rho} - \hat{\rho}\hat{H}, \tag{S7}$$

by applying the left vacuum $|I\rangle\rangle$ on both sides, we can find the time evolution equation for $|\rho\rangle\rangle$,

$$i\frac{d}{dt}\hat{\rho}\,|I\rangle\rangle = i\frac{d}{dt}|\rho\rangle\rangle = \hat{L}\,|\rho\rangle\rangle , \tag{S8}$$

with the Liouville operator, $\hat{L}$, which can be found from $[\hat{H},\hat{\rho}]\,|I\rangle\rangle$. Using the relationships, Eq. SM-II, and the Hamiltonian for SIAM,

$$\begin{aligned}\hat{H} &= \hat{H}_S + \hat{H}_{SB} + \hat{H}_B,\\ \hat{H}_S &= U\hat{n}_\uparrow\hat{n}_\downarrow + \sum_\sigma \varepsilon_\sigma \hat{n}_\sigma,\\ \hat{H}_{SB} &= \sum_{i,\sigma}\left(t_i\hat{c}^\dagger_{i,\sigma}\hat{d}_\sigma + \text{h.c.}\right),\\ \hat{H}_B &= \sum_{i,\sigma} E_i\hat{c}^\dagger_{i,\sigma}\hat{c}_{i,\sigma},\end{aligned} \tag{S9}$$

The corresponding Liouville operator can be found as,

$$\begin{aligned}\hat{L} &= \hat{L}_S + \hat{L}_{SB} + \hat{L}_B,\\ \hat{L}_S &= U\hat{n}_\uparrow\hat{n}_\downarrow - U(1-\hat{\tilde{n}}_\uparrow)(1-\hat{\tilde{n}}_\downarrow) + \sum_\sigma \varepsilon_\sigma(\hat{n}_\sigma + \hat{\tilde{n}}_\sigma),\\ \hat{L}_{SB} &= \sum_{i,\sigma}\left(t_i\hat{c}^\dagger_{i,\sigma}\hat{d}_\sigma + t_i\hat{\tilde{c}}^\dagger_{i,\sigma}\hat{\tilde{d}}_\sigma + \text{h.c.}\right),\\ \hat{L}_B &= \sum_{i,\sigma} E_i(\hat{c}^\dagger_{i,\sigma}\hat{c}_{i,\sigma} + \hat{\tilde{c}}^\dagger_{i,\sigma}\hat{\tilde{c}}_{i,\sigma}),\end{aligned} \tag{S10}$$

with constant terms omitted. For example, $\hat{\rho}c_i^\dagger c_j\,|I\rangle\rangle$ $(i\neq j)$ can be expressed as,

$$\hat{\rho}c_i^\dagger c_j\,|I\rangle\rangle = \hat{\rho}c_i^\dagger\tilde{c}_j\,|I\rangle\rangle = -\hat{\rho}\tilde{c}_j c_i^\dagger\,|I\rangle\rangle = \hat{\rho}\tilde{c}_j\tilde{c}_i^\dagger\,|I\rangle\rangle = -\tilde{c}_i^\dagger\tilde{c}_j\,|\rho\rangle\rangle\,. \tag{S11}$$

Note that the dynamics preserves its trace,

$$0 = i\frac{d}{dt}\,\mathrm{Tr}[\hat{\rho}] = \langle\langle I|\,\hat{L}\,|\rho\rangle\rangle\,, \tag{S12}$$

for any ρ, so $\langle\langle I|\,\hat{L} = 0$. This is the reason why $|I\rangle\rangle$ is called the left vacuum state.

SM-III. EVALUATION OF 1-RDM

A. Boundary IF-MPS

We first express $\hat{U}^{SB}$ in a single particle basis.

$$U^{SB} = \left(\begin{array}{c|c} K^{SS}_{ss'} & K^{SB}_{si'} \\ \hline K^{BS}_{is'} & K^{BB}_{ii'} \end{array}\right) \tag{S13}$$

Representing it in Grassmann variables, η and ξ,

$$\begin{aligned}\langle\bar{\eta},\bar{\xi}|\,\hat{U}^{SB}\,|\eta,\xi\rangle &= \exp\left[\bar{\eta}_s K^{SS}_{ss'}\eta_{s'} + \bar{\eta}_s K^{SB}_{si'}\xi_{i'} + \bar{\xi}_i K^{BS}_{is'}\eta_{s'} + \bar{\xi}_i K^{BB}_{ii'}\xi_{i'}\right]\\ &= \exp\left[\bar{\eta}_s K^{SS}_{ss'}\eta_{s'} + \bar{\xi}_i K^{BB}_{ii'}\xi_{i'}\right]\exp\left[\bar{\eta}_s K^{SB}_{si'}\xi_{i'} + \bar{\xi}_i K^{BS}_{is'}\eta_{s'}\right]\end{aligned} \tag{S14}$$

The terms, K^{SS} and K^{BB}, are factored out and the terms, K^{SB} and K^{BS}, couple S and B. K^{SB} and K^{BS} can be split with SVD, $K^{SB} = U^a\Sigma^a V^a$, $K^{BS} = V^b\Sigma^b U^b$. Using the resolution of identity,

$$\begin{aligned}\exp\left[\bar{\eta}_s K^{SB}_{si'}\xi_{i'}\right] &= \int\prod_p d\bar{\phi}^a_p d\phi^a_p \exp(-\bar{\phi}^a_p\phi^a_p)\exp\left[\bar{\eta}_s U^a_{sp}(\Sigma^a)^{1/2}_p\phi^a_p + \bar{\phi}^a_p(\Sigma^a)^{1/2}_p V^a_{pi'}\xi_{i'}\right],\\ \exp\left[\bar{\xi}_i K^{BS}_{is'}\eta_{s'}\right] &= \int\prod_p d\bar{\phi}^b_p d\phi^b_p \exp(-\bar{\phi}^b_p\phi^b_p)\exp\left[\bar{\xi}_i V^b_{ip}(\Sigma^b)^{1/2}_p\phi^b_p + \bar{\phi}^b_p(\Sigma^b)^{1/2}_p U^b_{ps'}\eta_{s'}\right],\end{aligned} \tag{S15}$$

$\hat{U}^{SB}$ can be expressed as,

$$\begin{aligned}\langle\bar{\eta},\bar{\xi}|\,\hat{U}^{SB}\,|\eta,\xi\rangle &= \exp\Big[\bar{\eta}_s K^{SS}_{ss'}\eta_{s'} + \bar{\eta}_s U^a_{sp}(\Sigma^a)^{1/2}_p\phi^a_p + \bar{\phi}^b_p(\Sigma^b)^{1/2}_p U^b_{ps'}\eta_{s'}\Big] \\ \times \int \mathcal{D}\bar{\phi}\mathcal{D}\phi \exp(-\bar{\phi}^a_p\phi^a_p - \bar{\phi}^b_p\phi^b_p) &\exp\Big[\bar{\xi}_i K^{BB}_{ii'}\xi_{i'} + \bar{\phi}^a_p(\Sigma^a)^{1/2}_p V^a_{pi'}\xi_{i'} + \bar{\xi}_i V^b_{ip}(\Sigma^b)^{1/2}_p\phi^b_p\Big],\end{aligned} \tag{S16}$$

where $\mathcal{D}\bar{\phi}\mathcal{D}\phi = \prod_p d\bar{\phi}^a_p d\phi^a_p \bar{\phi}^b_p d\phi^b_p$. It is equivalent to the contraction of two noninteracting gates, $\hat{U}^{SB} = \hat{W}^S \cdot \hat{W}^B$. $\hat{W}^S$ and $\hat{W}^B$ can be written in a single particle basis as follows,

$$W^S = \left(\begin{array}{c|c} K^{SS}_{ss'} & U^a_{sp}(\Sigma^a)^{1/2}_p \\ \hline (\Sigma^b)^{1/2}_p U^b_{ps'} & 0 \end{array}\right), \tag{S17}$$

$$W^B = \left(\begin{array}{c|c} 0 & (\Sigma^a)^{1/2}_p V^a_{pi'} \\ \hline V^b_{ip}(\Sigma^b)^{1/2}_p & K^{BB}_{ii'} \end{array}\right).$$

B. Iterative update of 1-RDM

The initial bath 1-RDM of the right IF state, Γ^R can be represented by a Slater determinant, C, after a purification,

$$C = \left[\begin{array}{c} \sqrt{\Gamma^R} \\ \hline \sqrt{I-\Gamma^R} \end{array}\right], \tag{S18}$$

which represents N_b occupied electrons in $2N_b$ orbitals and where the time evolution operator is applied to the first N_b orbitals. The time evolution operator can be either the Trotterized time evolution operator, $\hat{U}^{SB}$, or the boundary IF, $\hat{W}^B$. Here, we use the notation, $\hat{W}^B$, in a general sense, including both unitary and nonunitary time evolution ($\hat{W}^B$ in the boundary IF is nonunitary). We denote the single-particle representation of $\hat{W}^B$ as follows,

$$W^B = \left(\begin{array}{c|c} K^{SS}_{ss'} & K^{SB}_{si'} \\ \hline K^{BS}_{is'} & K^{BB}_{ii'} \end{array}\right). \tag{S19}$$

The column, $[K^{SB}, K^{BB}]^T$, is applied to the Slater determinant, and the other column, $[K^{SS}, K^{BS}]$, introduces additional occupied electrons. A transformed Slater determinant, C', is,

$$C' = \left(\begin{array}{c|c} K^{BB}\sqrt{\Gamma^R} & K^{BS} \\ \hline K^{SB}\sqrt{\Gamma^R} & K^{SS} \\ \hline 0 & I \\ \hline \sqrt{I-\Gamma^R} & 0 \end{array}\right). \tag{S20}$$

Note that each column is not normalized. To normalize the coefficient matrix, we compute the overlap matrix, $S = C^\dagger C$, and then the normalized Slater determinant can be expressed as, $C' = CS^{-1/2}$. The updated 1-RDM, Γ'^R is,

$$\Gamma'^R = \left(\begin{array}{c|c} K^{BB}\sqrt{\Gamma^R} & K^{BS} \end{array}\right) \cdot S^{-1} \cdot \left(\begin{array}{c} \sqrt{\Gamma^R}K^{BB\dagger} \\ \hline K^{BS\dagger} \end{array}\right) \tag{S21}$$

C. Gauge transformation of 1-RDM

Given the Slater determinant representation of the 1-RDM, as in Eq. S18, a gauge transformation, $\hat{G}$, is applied to the first N_b orbitals. The unnormalized gauge transformed Slater determinant, C_G, can be written as,

$$C_G = \left[\begin{array}{c} G\sqrt{\Gamma^R} \\ \hline \sqrt{I-\Gamma^R} \end{array}\right] \tag{S22}$$

and hence the overlap matrix is $C_G^\dagger C_G = \sqrt{\Gamma^R}G^\dagger G\sqrt{\Gamma^R} + I - \Gamma^R$. Therefore, the gauge transformed 1-RDM, Γ^G, is,

$$\Gamma^G = [C_G(C_G^\dagger C_G)^{-1}C_G^\dagger]_B = G\sqrt{\Gamma^R}(\sqrt{\Gamma^R}G^\dagger G\sqrt{\Gamma^R} + I - \Gamma^R)^{-1}\sqrt{\Gamma^R}G^\dagger \tag{S23}$$

In practice, we can construct the gauge transformed coefficient matrix and 1-RDM without the core and virtual basis in Γ^G with the eigenvalues $\lambda < \epsilon$ or $\lambda > 1-\epsilon$. We first construct C_G with the chosen basis and project out the gauge transformed core basis. The 1-RDM Γ^G is constructed afterward.

D. Equation of motion of 1-RDM in the continuous-time limit

In this section, we derive the equation of motion for the 1-RDM, Γ, in the continuous-time limit of the iterative 1-RDM update. In the continuous-time limit, $\Delta t \to 0$, and taking terms up to first-order in Δt, $\hat{W}^B$ has the following form,

$$W^B = \left(\begin{array}{c|c} 0 & -i\sqrt{\Delta t}K^{SB}_{si'} \\ \hline -i\sqrt{\Delta t}K^{BS}_{is'} & I - i\Delta t K^{BB}_{ii'} \end{array}\right). \tag{S24}$$

The updated Slater determinant is,

$$C' = \left(\begin{array}{c|c} (I - i\Delta t K^{BB})\sqrt{\Gamma^R} & -i\sqrt{\Delta t}K^{BS} \\ \hline -i\sqrt{\Delta t}K^{SB}\sqrt{\Gamma^R} & 0 \\ \hline 0 & I \\ \hline \sqrt{I-\Gamma^R} & 0 \end{array}\right). \tag{S25}$$

The overlap matrix from C' is

$$S = I + \sqrt{\Delta t}\begin{pmatrix} 0 & -i\sqrt{\Gamma^B}K^{BS} \\ iK^{BS\dagger} & 0 \end{pmatrix} + \Delta t \begin{pmatrix} \sqrt{\Gamma^R}(K^{SB\dagger}K^{SB} + iK^{BB\dagger} - iK^{BB})\sqrt{\Gamma^R} & 0 \\ 0 & K^{BS\dagger}K^{BS} \end{pmatrix} \tag{S26}$$

The updated 1-RDM, $\Gamma(t+\Delta t) = [C'S^{-1}C'^{\dagger}]_B$, is,

$$\begin{aligned} \Gamma(t+\Delta t) = \Gamma - i\Delta t K^{BB}\Gamma + i\Delta t \Gamma K^{BB\dagger} + \Delta t K^{BS}K^{BS\dagger} \\ -\Delta t K^{BS}K^{BS\dagger}\Gamma - \Delta t \Gamma K^{BS}K^{BS\dagger} + \Delta t \Gamma[K^{BS}K^{BS\dagger} - K^{SB\dagger}K^{SB} + i(K^{BB} - K^{BB\dagger})]\Gamma \end{aligned} \tag{S27}$$

In the continuous-time limit, the equation of motion is given by,

$$\frac{d\Gamma}{dt} = K^{BS}K^{BS\dagger} - i(K^{BB}\Gamma - \Gamma K^{BB\dagger}) - \{K^{BS}K^{BS\dagger}, \Gamma\} + \Gamma[K^{BS}K^{BS\dagger} - K^{SB\dagger}K^{SB} + i(K^{BB} - K^{BB\dagger})]\Gamma \tag{S28}$$

Given $\Gamma = \Gamma^R$, $K^{SB} = t^B$, $K^{BS} = t^{B\dagger}$, $K^{BB} = L_B$, with $L_B = L_B^\dagger$, and the equation of motion is given by,

$$\frac{d\Gamma^R}{dt} = t^{B\dagger}t^B - i[L_B, \Gamma^R] - \{t^{B\dagger}t^B, \Gamma^R\}. \tag{S29}$$

Given $\Gamma = \Gamma^L$, $K^{SB} = t^B$, $K^{BS} = t^{B\dagger}$, $K^{BB} = -L_B$, and the equation of motion is given by,

$$\frac{d\Gamma^L}{dt} = t^{B\dagger}t^B + i[L_B, \Gamma^L] - \{t^{B\dagger}t^B, \Gamma^L\}. \tag{S30}$$

Given $\Gamma = \Gamma^G$, $K^{SB} = \kappa^1$, $K^{BS} = \kappa^2$, $K^{BB} = L_{GB}$, and the equation of motion is given by,

$$\frac{d\Gamma^G}{dt} = \kappa^2\kappa^{2\dagger} - i(L_{GB}\Gamma^G - \Gamma^G L_{GB}^\dagger) - \{\kappa^2\kappa^{2\dagger}, \Gamma^G\} + \Gamma^G\left[\kappa^2\kappa^{2\dagger} - \kappa^{1\dagger}\kappa^1 + i(L_{GB} - L_{GB}^\dagger)\right]\Gamma^G \tag{S31}$$

E. Equation of motion of gauge transformation and effective orbital basis

The gauge transformation is expressed with the eigenvalues, ν_k, and eigenvectors, R^L_{ik}, of the left 1-RDM, Γ^L, $G_{ki} = g_k R^{L*}_{ik}$, where $g_k = \sqrt{\nu_k/(1-\nu_k)}$. Therefore, the equation of motion of the gauge transformation can be written in terms of $\dot{\nu}_k$ and $\dot{R}^L_{ik}$.

$$\left[\frac{d\hat{G}}{dt}\hat{G}^{-1}\right]_{kl} = \dot{g}_k g_k^{-1}\delta_{kl} - \sum_i g_k R^{L*}_{ik}\dot{R}^L_{il}g_l^{-1}, \quad \text{with} \quad \dot{g}_k g_k^{-1} = \frac{1}{2\nu_k(1-\nu_k)}\dot{\nu}_k. \tag{S32}$$

The time dependence of the eigenvalues and eigenvectors can be computed from the perturbation of Γ^L to $\Gamma^L - dt\dot{\Gamma}^L$ (the minus sign is from the fact that the left 1-RDM is propagated in the inverse time). Perturbation theory gives

the following expressions,

$$\begin{aligned}\dot{\nu}_k &= -\left[R^{L\dagger}\dot{\Gamma}^L R^L\right]_{kk} = -\sum_a |\sum_i t^B_{ai} R^L_{ik}|^2 (1-2\nu_k),\\ \left[R^{L\dagger}\dot{R}^L\right]_{kl} &= -\frac{\left[R^{L\dagger}\dot{\Gamma}^L R^L\right]_{kl}}{\nu_l-\nu_k}\ (k\neq l) = \frac{1-\nu_k-\nu_l}{\nu_k-\nu_l}\left[R^{L\dagger}t^{B\dagger}t^B R^L\right]_{kl} + i\left[R^{L\dagger}\hat{L}_B R^L\right]_{kl},\end{aligned} \tag{S33}$$

where $\dot{\Gamma}^L$ is given by Eq. S30.

The equation of motion of the effective orbital basis can be derived similarly, which contributes to the Liouville operator, $\hat{X} = -i\sum_{m,n}\left[R^{\text{eff}\dagger}\dot{R}^{\text{eff}}\right]_{mn}\hat{a}^\dagger_m\hat{a}_n$.

$$\left[R^{\text{eff}\dagger}\dot{R}^{\text{eff}}\right]_{mn} = \frac{\left[R^{\text{eff}\dagger}\dot{\Gamma}^G R^{\text{eff}}\right]_{mn}}{\tilde{\nu}_n-\tilde{\nu}_m}, \tag{S34}$$

where $\tilde{\nu}_m$ is the eigenvalue of Γ^G for the m-th effective orbital eigenvector.

F. Spectrum of Γ and Γ^G

Here, we prove certain properties of eigenvalues of Γ and Γ^G, namely that if ν is an eigenvalue of Γ or Γ^G, $1-\nu$ is also an eigenvalue of Γ or Γ^G. It is useful to start from the original density operator picture before the particle-hole transformation on one of the Fock spaces.

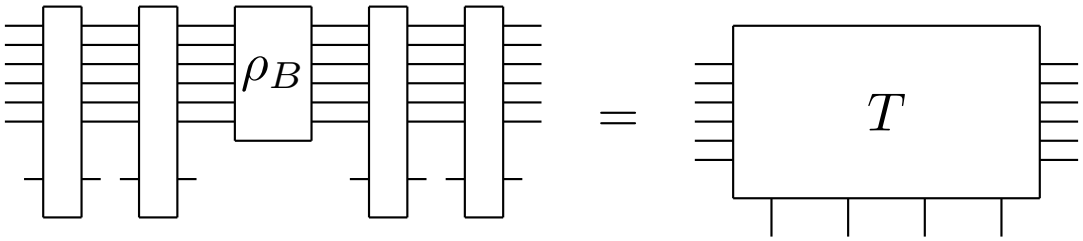

FIG. S7. Diagrammatic representation of tensor T, which refers to the tensor from a bipartite cut of the whole influence functional tensor before the k-th timestep ($k = 2$ in the figure).

First, to prove this property for Γ, we take the tensor, T, originating from a bipartite cut at the k-th timestep (Fig. S7), and represent it using Grassmann variables, η and ξ, which represent the impurity and bath, respectively.

$$T = \exp\left[\bar{\eta}_s g^{SS}_{ss'}\eta_{s'} + \bar{\eta}_s g^{SB}_{si'}\xi_{i'} + \bar{\xi}_i g^{BS}_{is'}\eta_{s'} + \bar{\xi}_i g^{BB}_{ii'}\xi_{i'}\right] \tag{S35}$$

We represent the phase in the exponential with the matrix G,

$$G = \left(\begin{array}{c|c} g^{SS}_{ss'} & g^{SB}_{si'} \\ \hline g^{BS}_{is'} & g^{BB}_{ii'} \end{array}\right). \tag{S36}$$

where Grassmann variables with bars (without bars) indicate fermions from the left (right) Hilbert space. From the nature of unitary time evolution, G is a Hermitian matrix, $G = G^\dagger$, and therefore diagonalizable, $G = U\Sigma U^\dagger$. After particle-hole transformation to the right Hilbert space, the tensor T can be represented as a Slater determinant,

$$|T\rangle = \prod_p \Big(\frac{\Sigma_p}{\sqrt{1+\Sigma_p^2}} f^\dagger_p + \frac{1}{\sqrt{1+\Sigma_p^2}}\tilde{f}^\dagger_p\Big)\,|0\rangle\,, \tag{S37}$$

where $f_p^\dagger$ and $\tilde{f}_p^\dagger$ are defined as follows,

$$\begin{aligned} f_p^\dagger &= U_{ip} c_i^\dagger + U_{sp} d_s^\dagger, \\ \tilde{f}_p^\dagger &= U_{ip} \tilde{c}_i^\dagger + U_{sp} \tilde{d}_s^\dagger. \end{aligned} \tag{S38}$$

The 1-RDM of the bath, Γ, corresponds to the 1-RDM expectation values of $c_i^\dagger$ and $\tilde{c}_i^\dagger$. Γ can be represented as,

$$\Gamma_{ij} = \left(\begin{array}{c|c} U_{ip}\frac{\Sigma_p^2}{1+\Sigma_p^2}U_{jp}^* & U_{ip}\frac{\Sigma_p}{1+\Sigma_p^2}U_{jp}^* \\ \hline U_{ip}\frac{\Sigma_p}{1+\Sigma_p^2}U_{jp}^* & U_{ip}\frac{1}{1+\Sigma_p^2}U_{jp}^* \end{array}\right) = \left(\begin{array}{c|c} M_1 & M_2 \\ \hline M_2 & M_3 \end{array}\right), \tag{S39}$$

where $M_3 = I - M_1$. Given this form, Γ satisfies $R\Gamma R^\dagger = I - \Gamma$, where $R = \begin{pmatrix} 0 & -I \\ I & 0 \end{pmatrix}$. Therefore, if v is an eigenvector of Γ with eigenvalue ν, Rv is also an eigenvector of Γ with eigenvalue $1-\nu$.

The spectrum of Γ^G can be similarly established by taking the IF tensor after tracing out the bath. The phase matrix G of the tensor is still a Hermitian matrix and hence the 1-RDM for the orbitals in one partition satisfies the same properties. The spectrum of Γ^G is the same as that of the 1-RDM of the partition from the IF tensor, so it also has eigenvalue pairs, ν and $1-\nu$.